Performance Evaluation of Electrothermal Anti-icing Systems for a Rotorcraft Engine Air Intake Using a Meta Model

SungKi Jung[§], L. Prince Raj[§§], A. Rahimi[‡], H. Jeong[†] and R. S. Myong[†,‡]

[§]Centro de Engenharia, Modelagem e Ciências Sociais Aplicadas, Universidade Federal do ABC, Santo André, São Paulo, 09210-580, Brazil

[§§]Department of Aerospace Engineering and Applied Mechanics, Indian Institute of Engineering Science & Technology, Shibpur, Howrah, 711103, India

[†]School of Mechanical and Aerospace Engineering, Gyeongsang National University, Jinju, Gyeongnam, 52828, South Korea

[‡]Research Center for Aircraft Core Technology, Gyeongsang National University, Jinju, Gyeongnam 52828, South Korea

Corresponding author R. S. Myong: *myong@gnu.ac.kr*

Abstract

A meta model was developed to evaluate the performance of electrothermal anti-icing systems for a rotorcraft engine air intake. A reduced-order model based on proper orthogonal decomposition and a general regression neural network was employed to build the meta model, which covered the entire envelope of icing conditions. A compressible Navier-Stokes-Fourier computational fluid dynamics code was used to simulate the three-dimensional airflow around the rotorcraft engine air intake. High-fidelity droplet trajectory and ice accretion codes were also used to calculate the collection efficiencies and ice accretions on the anti-icing surface of the engine air intake in the heat-on mode. By considering airfoil and rotorcraft engine air intake cases, a feasibility study was then conducted to assess the meta model, using the leave-one-out cross validation method. The module was updated using a self-organizing map that contained k-mean clustering for the new samples in the parametric space. Lastly, the performance of the electrothermal anti-icing system was evaluated to demonstrate the practical use of the meta model. The distributions of ice thickness and icing parameters on the anti-icing surfaces can be used as guidelines for determining the required level of heater power and the size of heat pads.

Keywords: Rotorcraft, Air intake, Meta model, Electrothermal anti-icing system, Critical icing condition

1. Introduction

A substantial amount of ice can form on the surfaces of rotorcraft engine intakes during flying through clouds containing supercooled water droplets, or during ground operations in inclement weather. Protection against ice accretion is necessary since ice formed near the engine intake may obstruct air flow and adversely affect engine performance [1]. This can occur when the obstruction significantly reduces the effective cross-sectional area of an inlet, thus reducing mass flow rate during engine operations. In addition, turbine blades or other internal engine components can be damaged by chunks of ice shed from the leading edge of the air intake or by runback ice entering along with airstream from beyond the anti-icing panels [2,3]. Those two cases and a rotorcraft anti- and de-icing system are illustrated in Fig. 1.

To avoid degraded engine performance and prevent the hazard of engine failure [4], proper ice protection systems (IPSs) are necessary. IPS design remains an important topic in aircraft design, and various strategies for ice protection have been developed in the past. These can be classified into two broad categories: de-icing and anti-icing approaches [5,6]. De-icing is the periodic shedding—either by mechanical or thermal means—of small ice buildups by destroying the bond between the ice and the protected surface. Anti-icing is the prevention of ice buildup on the protected surface, either by evaporating the impinging water or by allowing it to run back and freeze on noncritical areas. This is accomplished by evaporating supercooled water droplets that impinge on the surface or by exuding anti-icing fluids on a porous leading edge.

Ice protection systems are employed to improve the all-weather operational effectiveness of a helicopter fleet. They are required when helicopters operate in icing conditions during missions in winter, search and rescue missions, or offshore operations. The Eurocopter AS332 Super Puma helicopter is known to be the first rotorcraft certified for flight into known icing. However, icing certification of helicopters demands a significant amount of resources and time from manufacturers, requiring 3 plus winter seasons on average in natural icing flight testing, such as in the case of the Sikorsky UH-60 Black Hawk and the AgustaWestland EH1010 Merlin. For this reason, intense efforts are currently being undertaken in order to

reduce the time required for icing testing (or complete the natural icing campaign as planned) with the help of the high-fidelity analysis methods capable of accurately evaluating the performance of anti- and de-icing systems for a rotorcraft.

In this study, an electrothermal anti-icing system for the rotorcraft engine air intake is evaluated with the help of computational fluid dynamics (CFD) methods based on partial differential equations (PDE). Recently, CFD-based analysis methods [7-11] have played a growing role in the icing certification process. Liu *et al*. [10] presented a three-dimensional ice accretion model using the numerical solution of the unsteady Stefan problem. Raj *et al*. [11] investigated the sensitivity of ice accretion and degraded aerodynamic performance to the critical parameters affecting airfoil icing. They considered the sensitivity of eight ice shape attributes and ice mass to five critical physical and modeling parameters, including surface roughness and ice density.

For a safety analysis in aircraft icing, Wang *et al*. [12] proposed a method based on the fuzzy algorithm. Ayra *et al*. [13] proposed data-based, practical, and cost-effective mitigation measures to reduce the risk associated with erroneous total air temperature (TAT) measurements due to built-up high-altitude ice crystals. However, accurately evaluating the performance of three-dimensional anti-icing systems for an aircraft is still a challenging subject which needs further investigation. A notable example is the fatal accident of the AF447 flight, in the last decade, which was caused by elevated concentrations of high-altitude ice crystals. The ice crystals obstructed the pitot probes and induced the transmission of erroneous flight speed information to the auto-flight system [14]. When designing the pitot probe, the water concentration values were multiplied by a design margin factor of 2 with respect to the values in appendix C.

The anti- and de-icing mechanisms of hot air and electrothermal systems have been computationally modeled by several researchers in the past. Al-Khalil *et al*. [15,16] used a control volume energy analysis to evaluate a hot air anti-icing system for an engine inlet and nacelle. Keith *et al*. [17] modeled electrothermal icing systems using finite difference methods. Silva *et al*. [18] employed electrothermal de-

icing modeling and simulation to predict temperatures and runback water flow streamwise distributions on the airfoil surface. Wright *et al*. [19] and Nishio *et al*. [20] also conducted anti-icing analysis with ice accretion predictions as a tool for evaluating the performance of an electrothermal anti-icing system. Meanwhile, Lin *et al*. [21] developed superhydrophobic coatings for anti-icing applications and Shen *et al*. [22] studied the performance and applicability of ice phobic materials for anti-icing.

Even though CFD-based computational models for the anti-icing system have demonstrated a strong ability to deal with various icing conditions, vast computational resources are needed to process the high-fidelity CFD computations that are necessary to cover the whole icing envelope, as described in appendix C of the Title 14 Code of Federal Regulation (CFR), part 29 (or 25). The icing envelopes are defined in terms of pressure altitude, temperature, liquid water content (LWC), and the mean volume diameter (MVD) of water droplets for continuous maximum stratiform and intermittent maximum cumuliform clouds. Anti-icing simulations around the engine air intake in particular, as illustrated in Fig. 2, require several PDE-based high-fidelity calculations of air flow, droplet flow, and ice accretion with conjugate heat transfer at each condition in icing envelopes. As a result, efficient approaches based on lower-order approximations, like a meta model with the reduced-order model (ROM), are essential in aircraft icing certification and the design of ice protection systems.

The ROM can treat a complex system—for example, primitive variables of fluid flow on all grid points—by calculating a basis of vectors (modes) that represent the most relevant features of the system. A linear combination of these modes can also be used to cover all of the input domains. Among various techniques employed to compute the reduced-order basis of vectors [23], the proper orthogonal decomposition (POD) [24-27] has been shown to not only provide the optimal linear representation of the dominant features and physics but also to yield the truncation of the linear combination of modes for a given level of accuracy. Once the basis vectors are determined, the scalar coefficients in the linear combination of modes remain as discretized spaces where the empty spaces among the given input

parameters must be filled. Thus, a response surface method for the coefficients is required to replace the discretized spaces by continuous spaces.

Fortunately, the response surface can be obtained using various techniques, such as linear [28,29] or polynomial interpolation [30], Akima or Kriging interpolation [31], radial basis functions [32], or neural networks [33]. In particular, the general regression neural network (GRNN) based on memory, a branch of neural networks used for artificial intelligence, can provide estimates of continuous variables. This method can provide smooth transitions from one observed value to another, even with sparse data in a multidimensional space. It can thus be used for any regression problem in which the assumption of linearity is not justified [34,35]. Also, the GRNN can provide quick learning and fast convergence to an optimal regression surface as the number of samples becomes large.

Other crucial aspects of the meta model are that it provides an assessment of the accuracy of ROM solutions, and a selection of new samples to enhance accuracy. To assess the accuracy of ROM solutions, the leave-one-out cross validation (LOOCV) approach may be a good choice, since it does not need to calculate any additional samples from current samples [36]. For the selection of new samples, a self-organizing map (SOM) may serve as a clustering tool with the k-mean technique for the search [37] or an optimization algorithm [38,39]. Centroidal Voronoi tessellations [40] may also be used for the selection of new samples.

The present work aims to develop a meta model for efficiently predicting the thickness of ice accreted on the anti-icing surface around the rotorcraft engine air intake in the heat-on mode. The performance of the anti-icing system will then be evaluated using the meta model for the whole icing envelope. *Our study may be regarded as a first attempt to evaluate the performance of three-dimensional electrothermal anti-icing systems for a rotorcraft engine air intake over the entire icing envelope by developing a meta model consisting of POD, GRNN, LOOCV, and SOM modules, in conjunction with the high-fidelity air, droplet, and ice accretion codes.* Then, the information on ice thickness and corresponding parameters (MVD and

temperature) will be used in the design of a proper anti-icing system. Finally, the meta model will be used as a guideline for determining the required level of heater power and the size of heat pads.

In this study, among various types of rotorcraft engine intake [41], the Pitot-type intake using dynamic pressure in forward flight was considered. In the air calculation, a special boundary condition was imposed to adjust the pressure at a pressure-outlet zone of the engine air intake, to meet the desired mass flow rate. A state-of-the-art icing simulation CFD code, FENSAP-ICE [6], was used for the droplet impingement and ice accretion on the surface around the engine intake. This high-fidelity software based on partial differential formulations can concurrently solve the airflow over the airfoil, the formation of ice for given icing conditions, and the heat transfer from an IPS.

The droplet module, based on a Eulerian approach augmented by droplet-related continuity and momentum equations, was used to solve the partial differential equations for droplet velocity and concentration, using the airflow solution obtained from the air solver. The ice module also solved the partial differential equations for ice accretions and yielded the three-dimensional shape of ice and water film thickness on complex three-dimensional surfaces. Finally, a conjugate heat transfer module solved the coupled heat convection and conduction equations along with all the other modules to complete the simulation. For the meta model, the ROM based on the POD and GRNN was employed to obtain a basis of vectors and the scalar coefficient in the linear combination of modes. The LOOCV and SOM were used to assess the accuracy of the ROM and select the new samples, respectively.

The paper is organized as follows. Section II describes an entire procedure used to build the meta model for efficiently predicting the ice thickness on the anti-icing surface of the rotorcraft engine air intake. Section III presents a first validation of the CFD module for anti-icing simulations, by comparing with existing experimental data on airfoil and rotorcraft engine air intake. For validation, the meta model was then evaluated using a two-dimensional airfoil with an imposed anti-icing system. Section IV describes the strategy for determining anti-icing performance around the rotorcraft engine air intake needed to cover the entire ice envelopes.

Fig. 1. Rotorcraft anti- and de-icing systems and engine performance degradation by ice build-up.

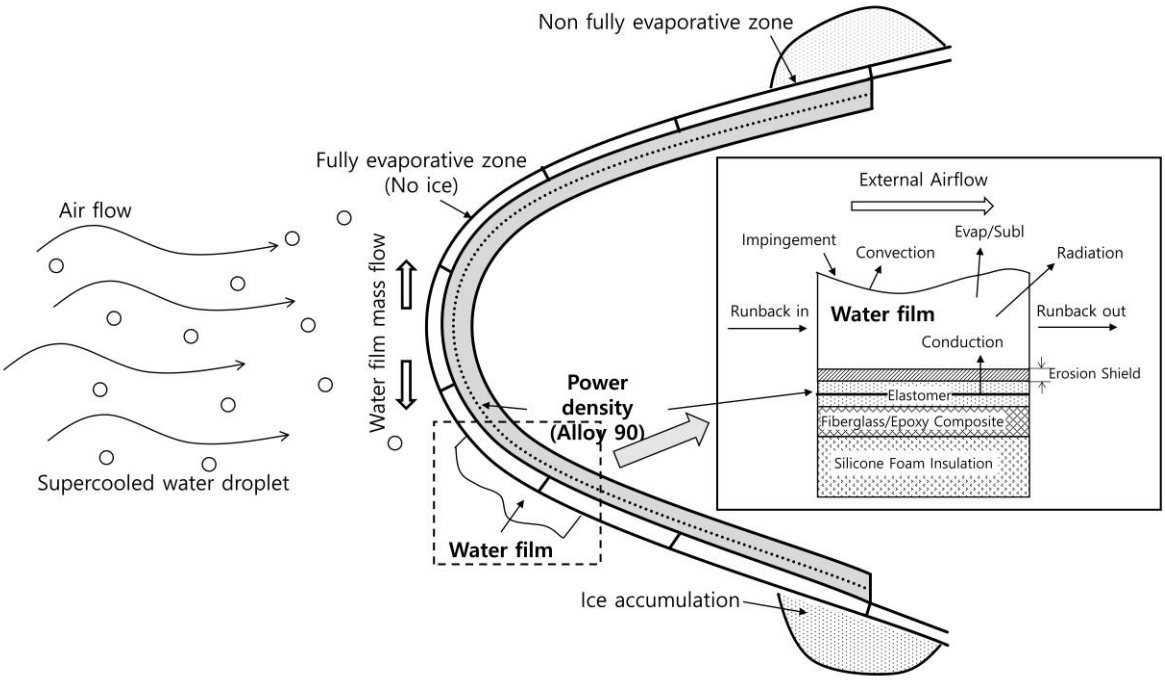

Fig. 2. A schematic of air-mixed droplet flows and ice accretion with conjugate heat transfer process over the anti-icing system.

2. Methodologies for the high-fidelity ice accretion and meta models

Generally, meta models based on the ROM for aircraft icing can be divided into two categories, global versus local approaches [36], due to the non-linear nature of ice shapes which can vary significantly depending on MVD, LWC, and temperature. However, when we consider the ice thickness on the electrothermal anti-icing surface in the heat-on mode, global ROM may be more suitable, since the ice thickness in that case is not significant, due to the high temperature produced inside the heat pads.

Figure 3 shows the entire procedure used to build the meta model. The CFD module determines the ice thickness on the anti-icing surfaces using each solver (air, droplet, and ice accretion). The main meta module based on the POD and GRNN with solutions provided by the CFD module is then activated to predict the ice thickness at arbitrary inputs. The solutions obtained by the meta module are evaluated using the LOOCV method. Once the error turns out to be acceptable, the meta model is completed. If not, the update module works to add new samples in parametric spaces using the SOM method. The new samples

become input parameters to the CFD module. This process is repeated until the error reaches a certain threshold. Each module adopted in the present work is briefly described in the following subsections.

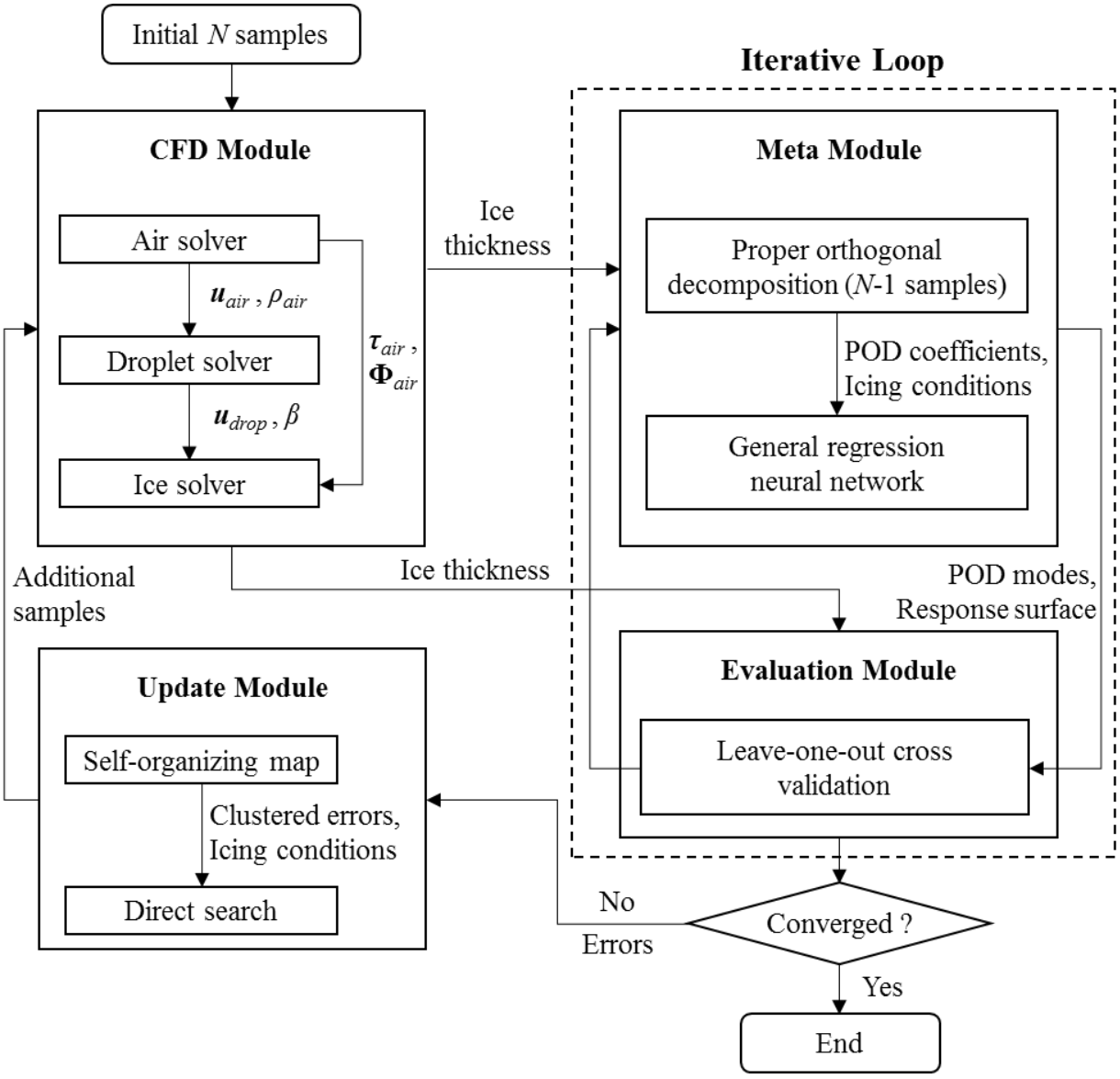

Fig. 3. A strategy for building the meta model.

2.1. CFD-based anti-icing module

The CFD module consists of three solvers, airflow, droplet, and ice accretion with conjugate heat transfer [6,42,43]. For the airflow solver, a compressible Navier–Stokes–Fourier code, ANSYS-FLUENT, based on the finite-volume method, was used. Roe's approximate Riemann solver is employed and extended to high-order accuracy with the least square method and Venkatakrishnan's limiter. The Spalart-Allmaras turbulent model for the Reynolds-averaged NSF equations was employed to simulate the turbulent viscous flow, since it is relatively simple and has been validated for external air flows [6]. For the droplet solver, droplet-related continuity and momentum equations in integral form were discretized to simulate the supercooled water droplet impingement on the anti-icing surface around the rotorcraft engine air intake [6]. DROP3D in the FENSAP-ICE code was used to deal with the complex three-dimensional droplet flow in a Eulerian frame. For the ice accretion solver, the ICE3D in the FENSAP-ICE code with the ability to treat conjugate heat transfer (CHT3D) was used to simulate ice thickness on the anti-icing surfaces around the rotorcraft engine air intake. The physical model employed in the ICE3D converts the classical algebraic Messinger ice model into partial differential equations of mass balance and heat transfer at the surface.

2.1.1. Air flow solver

The following compressible Navier-Stokes-Fourier equations were employed as the clean air solver,

$$\begin{bmatrix} \rho_g \\ \rho_g \mathbf{u}_g \\ \rho_g E \end{bmatrix}_t + \nabla \cdot \begin{bmatrix} \rho_g \mathbf{u}_g \\ \rho_g \mathbf{u}_g \mathbf{u}_g + p\boldsymbol{I} \\ (E+p)\mathbf{u}_g \end{bmatrix} = \nabla \cdot \begin{bmatrix} 0 \\ \boldsymbol{\tau} \\ \boldsymbol{\tau} \cdot \mathbf{u}_g + \mathbf{Q} \end{bmatrix}, \quad (1)$$

where ρ_g, $\mathbf{u}_g$, p, and E represent the density, the velocity, the pressure, and the total energy of the air, respectively. The non-conserved variables $\boldsymbol{\tau}$ and $\mathbf{Q}$ denote the viscous shear stress tensor and the heat flux vector, respectively. For air flow, the ideal equation of state $p = \rho_g RT$ and Sutherland's law of gas viscosity were assumed.

2.1.2. Droplet flow solver

The droplet flow solver is based on the Eulerian framework adopted in the CFD-based methods [6]. It is essentially a dilute two-fluid model (air and water) augmented by droplet-related continuity and momentum equations. In this solver, the following partial differential equations of water volume fraction and droplet velocity in the conservative form with source terms were solved:

$$\begin{bmatrix} \alpha \\ \alpha \mathbf{u}_d \end{bmatrix}_t + \nabla \cdot \begin{bmatrix} \alpha \mathbf{u}_d \\ \alpha \mathbf{u}_d \mathbf{u}_d \end{bmatrix} = \begin{bmatrix} 0 \\ C_D \dfrac{\alpha \mathrm{Re}_d}{24K} \left(\mathbf{u}_g - \mathbf{u}_d \right) + \alpha \left(1 - \dfrac{\rho_a}{\rho_w} \right) \dfrac{1}{Fr^2} \mathbf{g} \end{bmatrix}. \tag{2}$$

Here α and $\mathbf{u}_d$ are the non-dimensional water volume fraction and the velocity vector of the water droplet. C_D, Re_d, and K denote the drag coefficient, Reynolds number, and inertia parameter of the water droplet. Note that the equation of droplet velocity (2) is a convection-type equation with no diffusion terms. The term appearing in the right-hand side of the equation (2) represents the source effects which include the aerodynamic drag term described by an empirical drag coefficient for spherical droplets, gravity term, and the buoyancy term of the droplet. The local collection efficiency, which presents the droplet impingement on the solid surface, can be obtained from $\beta = -\alpha \mathbf{u}_d \cdot \mathbf{n}$, where $\mathbf{n}$ is a normal vector of the solid surface. The droplet impingement on the surface of the rotorcraft engine intake in the present study is simulated with the mono-disperse droplet assumption.

2.1.3. Ice accretion solver with the conjugate heat transfer

Under conditions of low ambient temperature, low speed, and low liquid water content, the droplets become ice instantly when they impinge on the solid surface, forming so-called rime ice. On the other hand, at warm ambient temperature, high speed, and high liquid water content, some portion of the droplets remains as water and moves on the surface. In glaze ice cases like this, information about shear stress and heat flux is essential, and a more complicated treatment of ice accretion is required. In order to simulate ice thickness on the complex geometry like the anti-icing surface around the rotorcraft engine intake, the

classical algebraic Messinger ice model was converted to partial differential equations of mass balance and heat transfer at the surface in this study:

$$\rho_w \left[\frac{\partial h_f}{\partial t} + \nabla \cdot \left(\bar{\mathbf{u}}_f h_f \right) \right] = U_\infty LWC\beta - \dot{m}_{evap} - \dot{m}_{ice}, \tag{3}$$

$$\begin{aligned} &\rho_w \left[\frac{\partial \left(h_f C_w \tilde{T} \right)}{\partial t} + \nabla \cdot \left(\bar{\mathbf{u}}_f h_f C_w \tilde{T} \right) \right] = \left[C_w \tilde{T}_{d,\infty} + \frac{\left| \mathbf{u}_d \right|^2}{2} \right] U_\infty LWC\beta - \frac{\left(L_{evap} + L_{subl} \right)}{2} \dot{m}_{evap} \\ &+ \left(L_{fusion} - C_{ice} \tilde{T} \right) \dot{m}_{ice} + \varepsilon\sigma \left[\left(\tilde{T}_\infty + 273.15 \right)^4 - \left(\tilde{T} + 273.15 \right)^4 \right] - C_h \left(\tilde{T} - \tilde{T}_{\infty_0} \right) + Q_{anti-icing}. \end{aligned} \tag{4}$$

The ice accretion model solves the mass and energy balance along the surface to predict the amount of water accumulation $\dot{m}_{ice}$ and equilibrium temperature $\tilde{T}$. The unfrozen water is considered runback water, and the velocity of the water film $\bar{\mathbf{u}}_f$ can be represented as a function of the water film thickness h_f and shear stress τ_{wall} as follows,

$$\bar{\mathbf{u}}_f (\mathbf{X}) = \frac{h_f}{2\mu_w} \tau_{wall} (\mathbf{X}). \tag{5}$$

In equations (3), (4) and (5), μ_w, C_w, C_{ice}, C_h represent the dynamic viscosity, the specific heat at constant pressure for water, and specific heat at constant pressure for ice, and the convective heat transfer coefficient, respectively [6]. The instantaneous evaporation mass, latent heat of fusion, latent heat of evaporation, and latent heat of sublimation are represented by $\dot{m}_{evap}, L_{fusion}, L_{evap}, L_{subl}$ respectively. Further, $\tilde{T}_\infty$ and $\boldsymbol{u}_d$ represent droplet temperature in degrees Celsius and the droplet impact velocity vector, respectively. The terms ε and σ represent the solid emissivity and Boltzmann constant (σ = 1.38064852 × 10^{-23} m^2 kg s^{-2} K^{-1}), respectively. In this process, the following compatibility conditions are needed:

$$h_f \geq 0,\ \dot{m}_{ice} \geq 0,\ h_f \tilde{T} \geq 0,\ \dot{m}_{ice} \tilde{T} \leq 0. \tag{6}$$

Note that $Q_{anti\text{-}icing}$ in equation (4) plays an essential role in the conjugate heat transfer, which involves thermal interaction between the solids (electrothermal heater pad) and fluids (supercooled water droplet and air). For ice accretion without heat sources, the adiabatic wall boundary condition for temperature is

imposed to $Q_{anti\text{-}icing}$, that is, $Q_{anti\text{-}icing}$=0. Otherwise, ice accretion with heat sources involves heat conduction governed by the following partial differential equations,

$$\frac{\partial H_M(T)}{\partial t} = \nabla \cdot \left(k_M(T) \nabla T \right) + S_M(t) \ , \tag{7}$$

where the subscript M denotes the solid material type, and H_M and k_M are the material enthalpy and the thermal conductivity, respectively. S_M represents the volumetric heat source generated by the heater films. The dependent variable T represents the solid material temperature, and t denotes the time [44]. The temperatures of $\widetilde{T}$ and T obtained from equations (3-4) and (7) are used to provide $Q_{anti\text{-}icing}$ using

$$Q_{anti-icing} = -Ak_M \frac{\partial T}{\partial \boldsymbol{n}} \ . \tag{8}$$

Here, $\boldsymbol{n}$ and A denote the normal vector and the area of the boundary surface, respectively. ∂T is determined by $\tilde{T}$ and T.

In principle, the electrothermal anti-icing analysis requires unsteady calculations in which all solvers interact during the simulation. The ice thickness on the solid surface is obtained with the time-accurate calculation. However, using fully coupled unsteady simulations to cover the entire icing envelope is unrealistic, especially for the three-dimensional complex geometry. For this reason, in practice, the external flow domains (air and droplet flows), which consume most of the computing time, are assumed to remain unchanged in a steady state. Only the ice accretion process with conjugate heat transfer is assumed unsteady, and the steady-state solutions obtained with the air and droplet solvers are inserted into the ice accretion with conjugate heat transfer as inputs.

2.2. Meta module

The POD for ROM is a procedure that provides an optimal orthonormal set of basis vectors for a given ensemble of data. The objective is to yield a set of a basis vector, Φ, of length n for an ensemble of data, $\mathbf{Y}=(\mathbf{Y}_1, \mathbf{Y}_2, \ldots, \mathbf{Y}_m)$, where $\mathbf{Y}_i=(y_{i1}, y_{i2}, \ldots, y_{in})$. For continuous spaces, such as icing envelopes, n can be

very large, and the solution of the corresponding eigenvalue problem can be prohibitively expensive. To avoid this problem, Sirovich [25] introduced the method of snapshots (an $N \times N$ matrix, where N is the number of snapshots in the ensemble of data) instead of solving an $n \times n$ matrix for the eigensystem. The POD basis modes are written in terms of the members of the ensemble data and eigenvector of the correlation matrix $Y_i^T Y_j / N$,

$$\Phi_i = \sum_{i=1}^{N} v_i Y_i, \tag{9}$$

where v_i is the eigenvector of the correlation matrix. Among every POD basis mode, only M number of available modes are chosen by energy level. Then, a reduced-order model with a reduced subspace defined by an energy level, $Y^{POD}=(\Phi_1, \Phi_2, \ldots, \Phi_M)$, can be obtained,

$$Y^{POD} = \sum_{i=1}^{M} a_i' \Phi_i, \tag{10}$$

where a_i' represents the POD coefficient defined as $\frac{y_i \Phi_i}{\Phi_j \Phi_i}$, Φ_i represents the i^{th} POD basis mode, and M indicates the truncation of the expansion at the desired level of energy content. The fraction of the total energy associated with each mode Φ_i can be computed,

$$E = \sum_{j=1}^{M} \lambda_j \Big/ \sum_{i=1}^{Ns} \lambda_i, \tag{11}$$

where λ, Ns denote an eigenvalue and the total number of snapshots, respectively. When considering the POD for the present problem, the CFD solutions at grid points and the corresponding icing conditions can be treated as $\mathbf{Y}$ and N, respectively.

Reduced-order models based on the POD, used to cover the parametric space from the discrete sample space to a continuous space, require a response surface model for the coefficients, a_i'. For this purpose, the GRNN [30], consisting of a memory-based network, is used to provide estimates of the coefficients in a continuous space. The general architecture of the GRNN is illustrated in Fig. 4. $\mathbf{X}=[X_1, X_2, \ldots, X_k]^T$, where k is a number of snapshots, are the input parameters (like the MVD and LWC) in discretized spaces, and $\hat{y}$

are the GRNN estimate of the actual output y, which are the POD coefficients corresponding to the input parameters. $\mathbf{X}^j=[X_1^j, X_2^j,\cdots, X_k^j]^{\mathrm{T}}$ and y^j for j=1, …, l, where l is the number of observations, are the observed input and output data to form pattern units. The GRNN estimate $\hat{y}$ can be expressed using A and B in the summation units,

$$\hat{y}(\mathbf{X},h)=\frac{A}{B}=\frac{\sum_{j=1}^{l} y^j \exp\left(-\frac{1}{2}\sum_{i=1}^{k}\frac{\left(\mathbf{X}_i-\mathbf{X}_i^j\right)^2}{h_i^2}\right)}{\exp\left(-\frac{1}{2}\sum_{i=1}^{k}\frac{\left(\mathbf{X}_i-\mathbf{X}_i^j\right)^2}{h_i^2}\right)}, \tag{12}$$

where h is a smooth parameter (bandwidth). In order to predict the POD coefficients in a continuous space, a smooth parameter of GRNN can be obtained by training the neural network. The number of input data in the input layer and the corresponding output data are gradually increased when building the meta model.

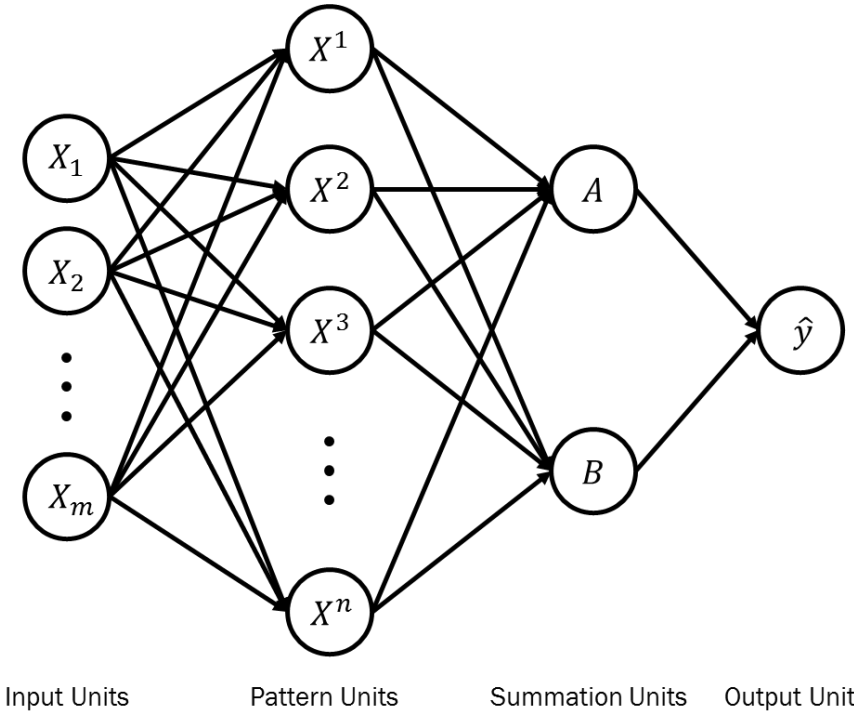

Fig. 4. General architecture of the general regression neural network (GRNN) [30].

2.3. Evaluation module

The accuracy of the solutions obtained using the meta model can be evaluated by directly comparing them with the corresponding full-order CFD solutions via a leave-one-out cross-validation approach (LOOCV) [36]. Given a set of *Ns*-number of snapshots obtained with the CFD simulations, one of the snapshots is selected as a reference solution. The other snapshots, *Ns*-1, are used to build the meta model. Then, a solution obtained by the meta model under the reference condition is compared with the reference solution. Errors between the meta solutions and CFD solutions at a given reference point are evaluated, and then another snapshot is selected as a new reference to evaluate the meta model. This process is repeated until all of the snapshots are evaluated over the entire parametric space. Since this approach does not need any additional sample to evaluate the meta model, the computational cost for evaluating the meta model is equivalent to building the meta model with *Ns* snapshots. In addition, building the meta model this way is cost-effective, since each meta model via *Ns*-1 snapshots chosen from *Ns* snapshots is decoupled, and can be easily parallelized. In this study, the thickness of the ice accreted on the anti-icing surface in the heat-on mode is of primary interest, and thus the accuracy of the meta model can be evaluated using the maximum difference in the ice thickness of the meta and the CFD solutions at each grid point on the anti-icing surface. During the iteration process, the number of snapshots will be increased to the level that is sufficient to provide a reliable error estimation.

2.4. Update module

Defining a suitably rich set of snapshots in the parametric space is a critical issue in the proper design of experiments. Errors obtained with the evaluation module in parametric space can provide information about error distributions in selected samples, but the information for newly added samples is still ambiguous. This naturally leads to questions about how many samples should be added and where to locate the samples in the parametric space.

To this end, a proper sampling method is required to select new samples. For the sampling method, using a clustering method which can identify the interactions between the input and output data may play an important role in searching for new samples and understanding the behavior of the system. In this study, a self-organized map (SOM) [45] is employed to cluster the errors and add the new samples. The SOM is one of the neural network models [46], and the algorithm is based on unsupervised and competitive learning. It provides a topology preserving mapping, meaning that nearby points in the input space are mapped to nearby units in the SOM from the high dimensional space to map units. Since map units, or neurons, usually form a 2-D lattice, the SOM is mapping from high dimensions to two dimensions. The SOM can serve as a cluster analysis tool for high-dimensional data. In the SOM module the new samples are chosen with a k-mean clustering technique. The process is repeated until the largest difference reaches a certain threshold.

3. Validations and evaluations

The reliability of the meta model depends on the accuracy of submodules. In particular, the accuracy of the CFD module that provides original sources of data set must be guaranteed in order to build a reliable meta model.

In this section, the CFD module for anti-icing is validated using a two-dimensional airfoil [47] and three-dimensional rotorcraft engine air intake [6]. The meta model is then evaluated by comparing the ice thickness results from the meta and CFD solutions.

3.1. Two-dimensional airfoil

The CFD solutions for the two-dimensional anti-icing simulations were validated using experimental data [47]. The anti-icing experiments were performed at the Icing Research Tunnel in the NASA Glenn Research Center, and surface temperatures were measured to validate the LEWICE/ANTICE code. A NACA 0012 airfoil with 72 inches span by 36 inches chord was equipped with electronically-controlled heat pads installed with a thermocouple, thermo-resistor sensor, and heat flux gauge in the streamwise

direction. The protected area was 7.75 inches streamwise (upper and lower surfaces at the leading edge). Figure 5 shows a schematic of the cross-section of the experimental model. The power density, length of each heating pad, and material properties are summarized in Tables 1 and 2. The initial conditions for the airflow, droplet flow, and ice accretion are also given in Table 3.

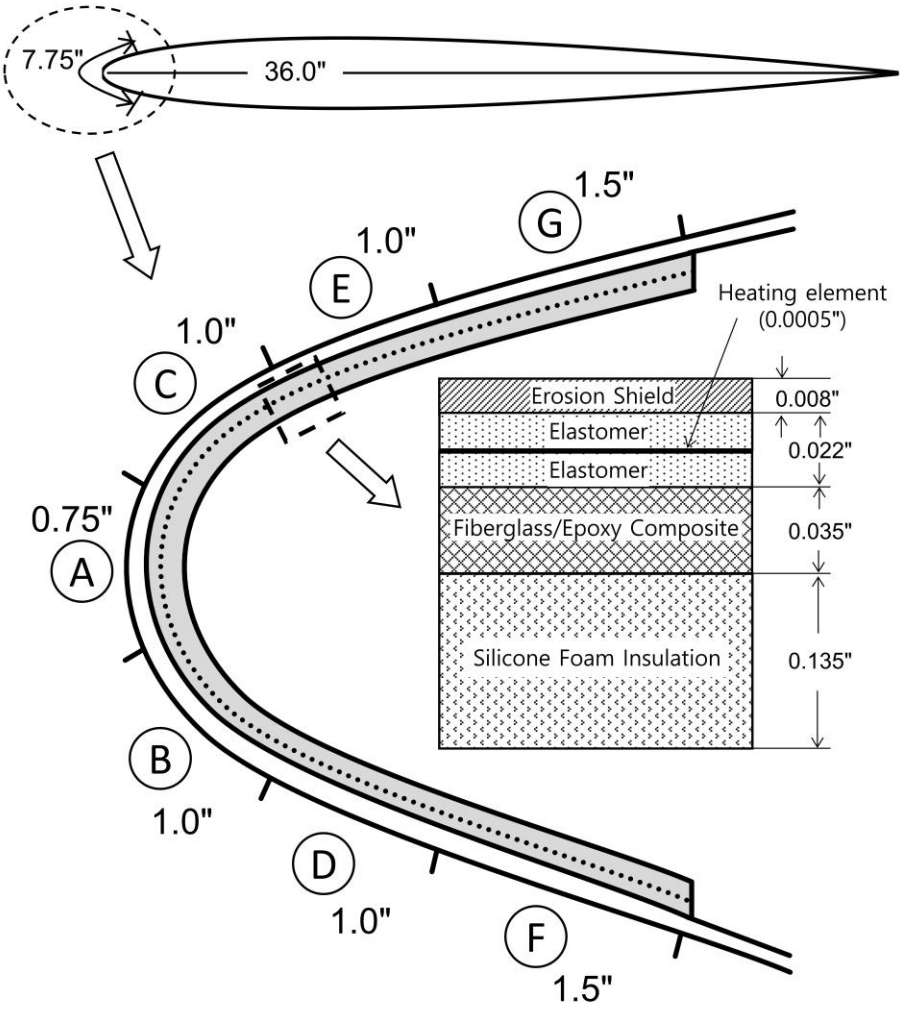

Fig. 5. A schematic of the cross-section of airfoil leading edge and heat pad.

Table 1 Heater power densities.

Zone	Power density (W/in^2)
A	3.1
B	2.6
C	1.9
D	1.9
E	2.2
F	1.7
G	1.5

Table 2 Leading edge material properties.

Material	K (Btu/hr·ft·°F)	P (lbm/ft^3)	C_p (Btu/lbm·°F)
Heating element (alloy 90)	23.7	556	0.092
Erosion shield (SS 301 HH)	9.4	501	0.12
Elastomer (Cox 4300)	0.148	86.4	0.30+/-0.03
Fiberglass/epoxy composite	0.17	112	0.375
Silicone foam insulation	0.07	40.5	0.27+/-0.03

Table 3 Icing conditions for a NACA 0012 airfoil.

T_{tot} (°F)	V (mph)	LWC (g/m^3)	MVD (μm)	AoA (degree)
20	100	0.78	20	0

The grid for air flow around the NACA 0012 airfoil was generated by C-type mesh with 132,160 cells, as shown in Fig. 6. Solid meshes for the layers of heat pads were generated by quadrilateral mesh with 33,976 cells. Inflow, outflow, and no-slip boundary conditions were imposed on the far-field and solid surface, respectively. The height of the first cell near the solid surface was set at $y+ \sim 1$ to accurately capture the behaviors of the viscous flow, where shear stress on the solid surface plays a key role in determining the convective flux in the continuity and energy equations within the ICE3D module. Figure 7 shows the distribution of the pressure coefficients and shear stresses (skin friction coefficients) on the airfoil surface. The results are in good agreement with the experimental data and the predictions of another CFD code [48].

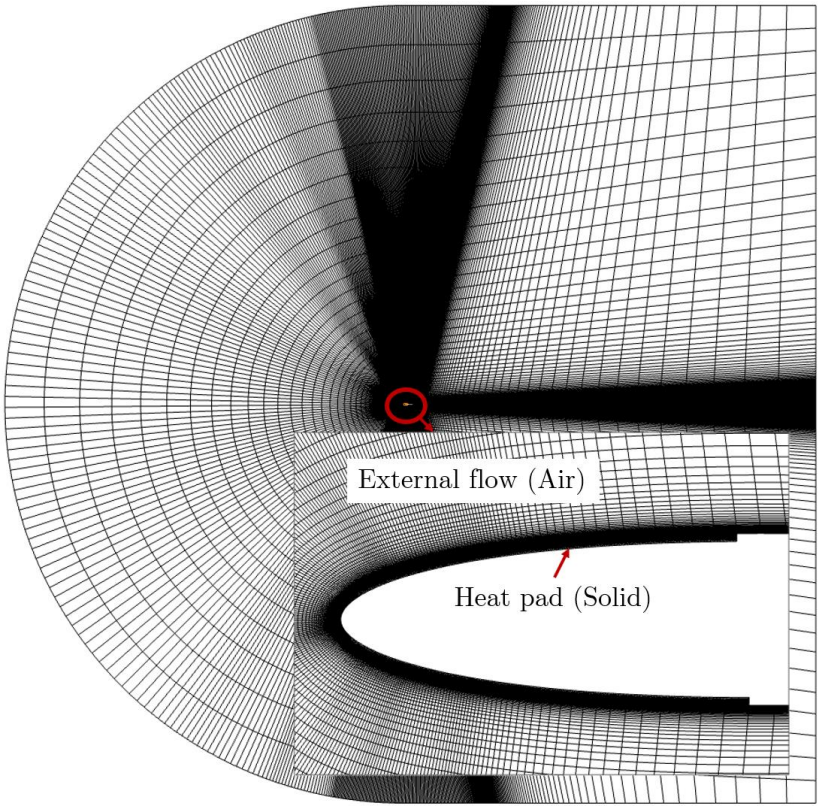

Fig. 6. Grid topology with boundary conditions, mesh distributions for external flow (air-mixed droplet flows) and heat transfer (heat pad).

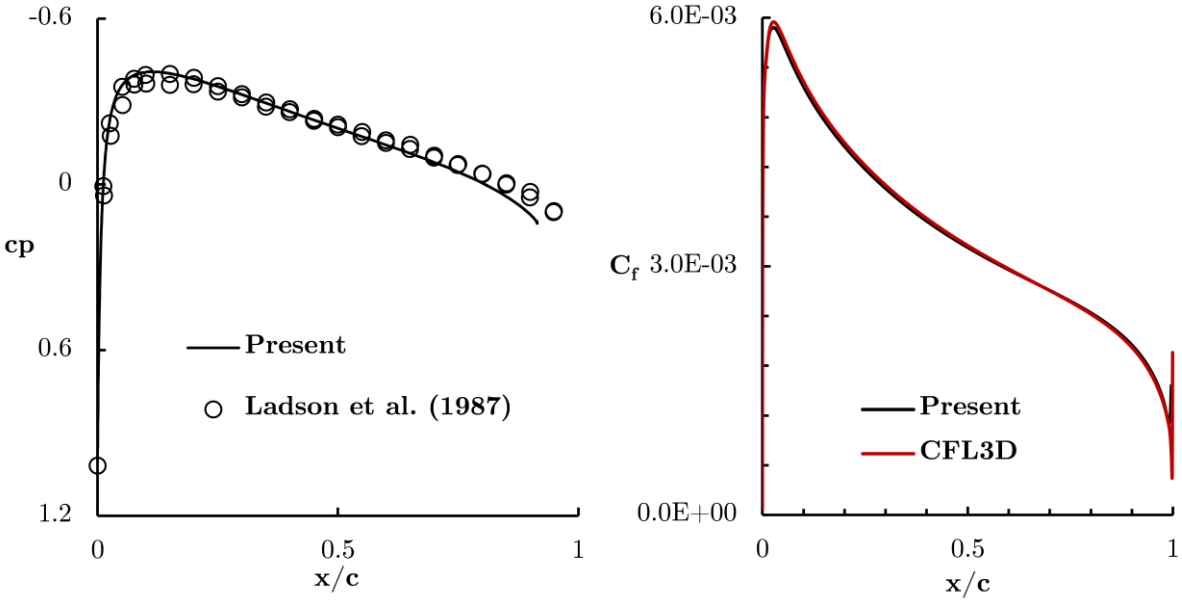

Fig. 7. Pressure coefficients (left) and skin friction coefficients (right).

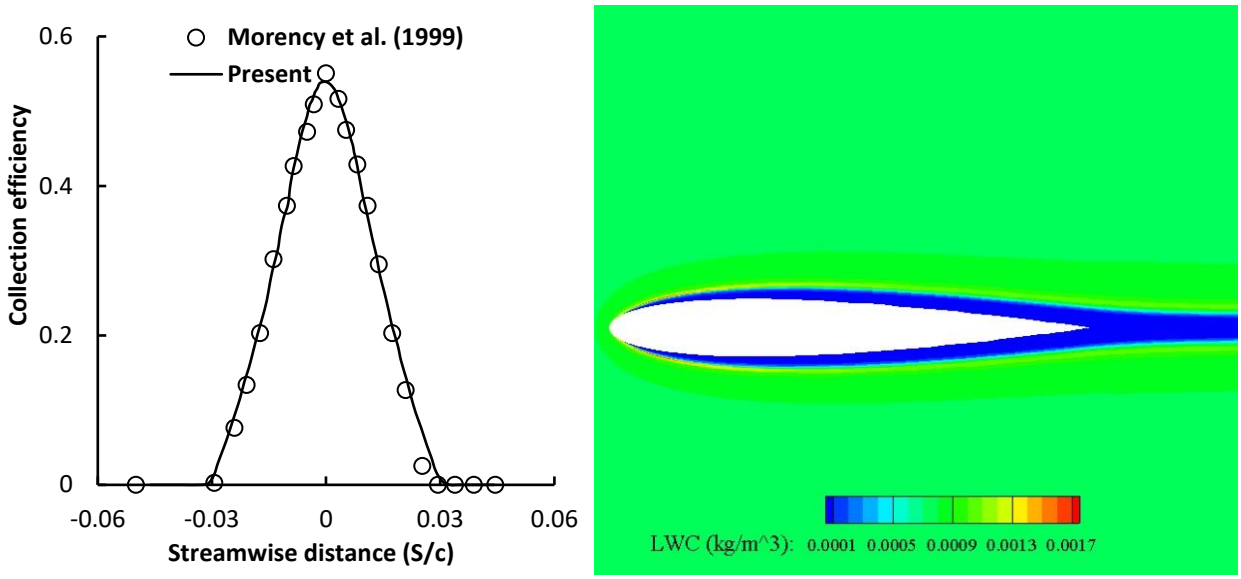

Fig. 8. Collection efficiency (left) and LWC distributions around a NACA 0012 airfoil (right).

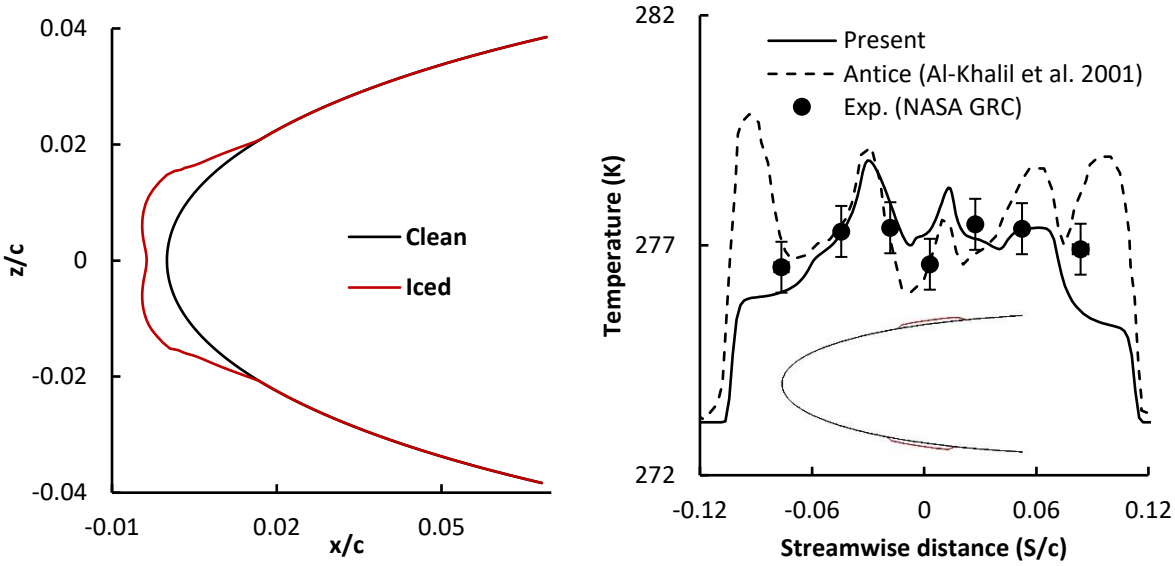

Fig. 9. Ice shapes (heat-off mode, left) and surface temperatures (heat-on mode, right) of experimental data and CFD simulations.

Figure 8 shows the distribution of collection efficiency and LWC around the airfoil for mono-dispersed supercooled droplet. The collection efficiency and impingement limits were in close agreement with experimental data, and shadow zones could be clearly identified from the LWC distributions on the upper

and lower sides of the airfoil. Figure 9 shows the ice shapes in the heat-on and heat-off modes and the surface temperature distribution on the surface of the airfoil in the heat-on mode. In Fig. 9 (left), the ice shapes predicted by present CFD solvers are shown to illustrate the performance of the anti-icing system.

In the heat-on mode, time sequences were ignored, since the current simulation is focused on the anti-icing system, not the de-icing system. The predicted maximum temperature was approximately 280 Kelvin over the whole heat pads for an exposure time of 600 seconds. Temperature distributions in the CFD simulations were found to be in qualitative agreement with the experimental data. The temperature drop near the stagnation point is due to evaporative cooling. Runback ices were observed after the anti-icing surfaces in the heat-on mode, even though their thickness turned out to be negligible. The discrepancy in the surface temperature at s/c=0.08 may be due to the absence of the rivulet model in our CFD module, which plays a non-negligible role in the runback flux in the icing process [49].

3.2. Three-dimensional rotorcraft engine air intake

There are very few experimental studies on the performance of anti-icing systems on three-dimensional set-ups. Here we considered a three-dimensional rotorcraft engine air intake [6] to validate the meta model of the anti-icing system. The experimental work was performed at the Centro Italiano Ricerche Aerospaziali (CIRA) Icing Wind Tunnel in 2012. This closed type of wind tunnel with dimensions of 2.6m x 3.8m x 9.9 m is considered one of the most modern (opened in 2002) facilities capable of reproducing realistic flight conditions inside a cold cloud in a controlled and repeatable environment. In order to avoid the problem of scaling laws, a full-scale model of the rotorcraft engine intake was manufactured and tested with an air suction system and with associated control units monitoring the correct mass flow rate in the intake.

The engine intake, nacelle, the environmental control system, and icing wind tunnel were considered when defining the computational domain. To include the interactions between the air intake model and the icing wind tunnel wall, the outside boundaries of the computational domain were treated as a solid surface

with the no-slip condition. It was expected that a non-negligible effect exists, associated with blockage space between the test model and the icing wind tunnel wall.

Figure 10 shows the overall configuration of the engine intake model used in the wind tunnel test. The solid lines near the engine intake represent the boundary of the heat pad of the electrothermal anti-icing system. To meet the targeted mass flow rate, which generally varies depending on engine operating modes, the pressure at the pressure-outlet zone of the engine air intake was adjusted at every iteration using the relation, $dp = \frac{\rho_{ave}\left(\dot{m}^2 - \dot{m}_{req}^2\right)}{2\left(\rho_{ave}A\right)}$, where $\dot{m}$ and $\dot{m}_{req}$ denote the computed and required mass flow rates, respectively, and A is the area of the pressure-outlet boundary, and ρ_{ave} is the computed average density at the pressure-outlet boundary.

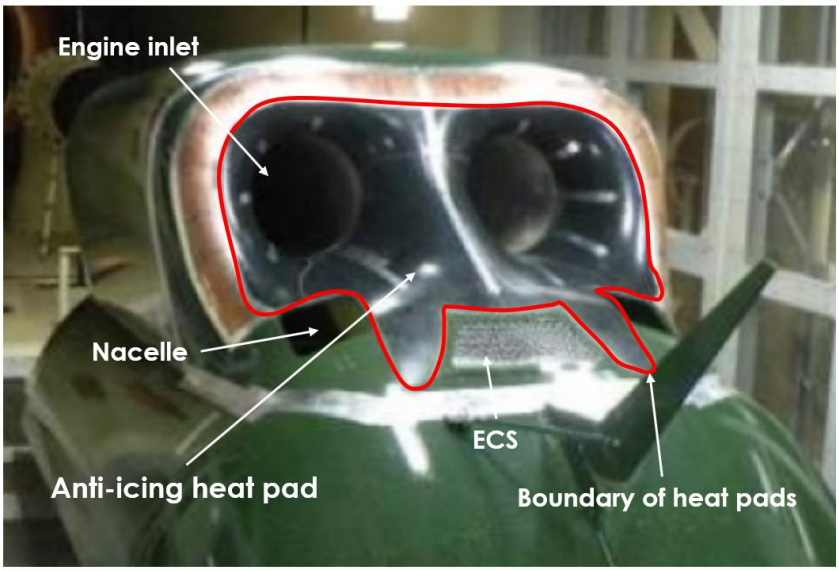

Fig. 10. Overall configurations of the rotorcraft engine air intake model used in the icing wind tunnel test.

Table 4 Icing conditions (at sea level) for the rotorcraft engine air intake.

Case	T_{tot} (K)	V(m/s)	LWC(g/m^3)	MVD(μm)	Slip angle (degree)
1	263	65	0.6	20	-2
2	255	72	0.3	20	-2

The icing conditions used for the wind tunnel tests of the rotorcraft engine air intake are given in Table 4. A -2-degree sideslip angle was imposed to take into account the effect of rotor blade downwash within the space limitation of the wind tunnel test section. The target mass flow rate at the end of the engine intake was set 3.8 kg/sec. Cases 1 and 2 in Table 4 represent the intermediate (or close to glaze) and rime icing conditions, respectively.

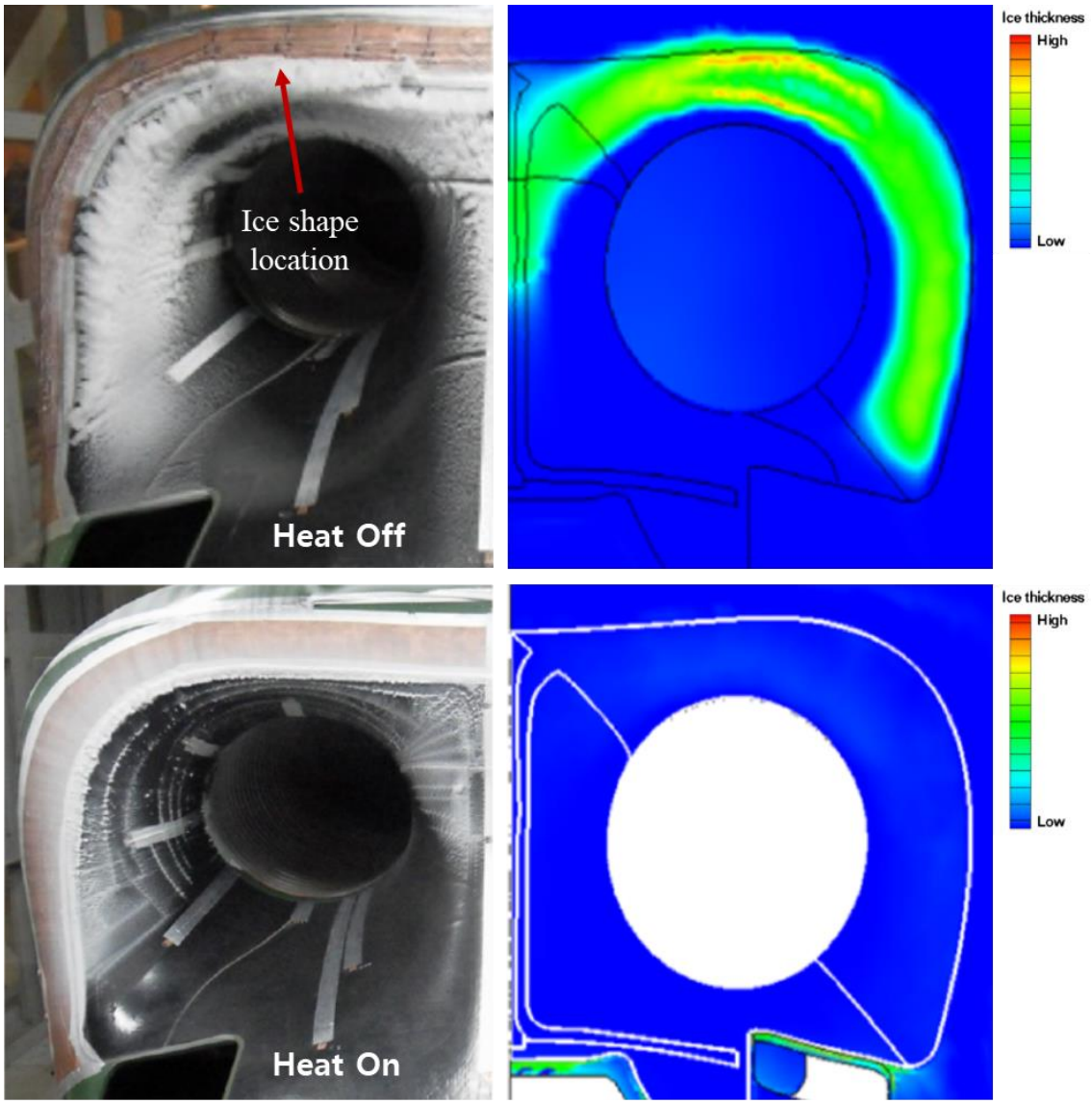

Fig. 11. Comparison of experimental image data of accumulated ices and simulated ice shapes in the heat-off (case 1 with exposure time 1,800 seconds, upper) and heat-on (case 2, lower) modes [6].

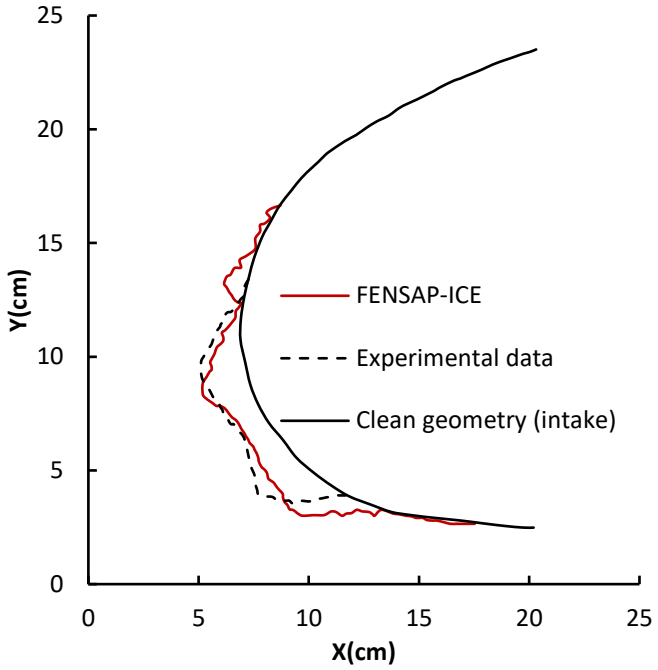

Fig. 12. Comparison of cross-sectional ice shapes (case 1 with exposure time 1,800 seconds) [6].

Figure 11 shows the comparison of experimental image data of accumulated ices and simulated ice shapes in the heat-off and heat-on modes. In the heat-off mode, two peaks exist at the inner part of the air intake lip, and a region with very thin flat ice accumulation between these peaks was clearly found in both the computational and experimental results. In the heat-on mode, the simulated ice thickness on the anti-icing surface was almost negligible, and such behavior was confirmed in the experimental image data. Further, the cross-sectional shape of accumulated ices at the ice shape location shown in Fig. 11 was measured by hand drawing during the icing wind tunnel test, as shown in Fig. 12, and reproduced from the previous work [6]. The comparison of ice shapes clearly shows that the computational results are in qualitative agreement with the experimental data in terms of the range and shape of ice. In summary, the accuracy of the CFD module for building the meta model was successfully validated by comparing with experimental data.

3.3. Transformation of ice thickness into ice shapes

When constructing a meta model of ice shapes, two choices are available, a coordinate-based meta model and a thickness-based meta model. Zhan *et al.* [50] used the coordinate-based meta model for predictions of ice shapes. In this work, we propose a new meta model based on the thickness of the ice. In the coordinate-based meta model, two or three different meta models must be built for the two or three-dimensional (*x*, *y*, and *z* coordinates) ice shapes. The increase in the number of sets of meta models increases the complexity of the meta model. In contrast, the thickness-based meta model requires only one set of meta model by removing the dimensions as scalar values on each node. The directional information missing in the ice thickness (scalar) can be provided by defining the ice shape (vector) using grid information, as illustrated in Fig. 13.

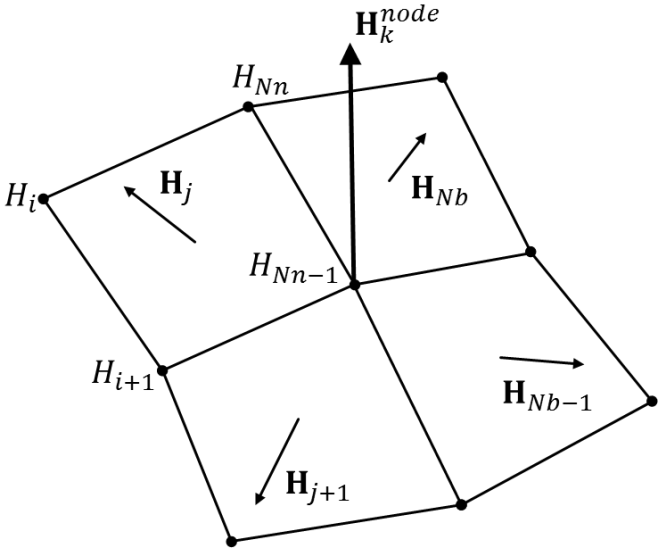

Fig. 13. Transformation of ice thickness (scalar) into ice shapes (vector) using grid information.

The ice thickness on the nodes is transferred into the cell center through a relation of each thickness, $\bar{H}_j = \frac{1}{Nn}\sum_{i=1}^{Nn} H_i$, where $\bar{H}$ is an average of the ice thickness at the cell center, $j = 1, \cdots, Nc$, Nc is the number of cells on the surface meshes, and Nn is the number of nodes surrounding the cell (Nn=3 for triangular mesh, Nn=4 for quadrilateral mesh). Then, the ice shape on the cell center can be determined by

the mean of ice thickness and normal vector on the cell center, $\mathbf{H}_j = \bar{H}_j \cdot \mathbf{n}_j$, where $\mathbf{H}_j$ indicates the ice shape on the cell center, and $\mathbf{n}_j$ is the normal vector on the cell center. Lastly, the *k*-th ice shape on the node $\mathbf{H}_k^{node}$ is determined by an average of $\mathbf{H}_j$ surrounding the node, $\mathbf{H}_k^{node} = \frac{1}{Nb}\sum_{j=1}^{Nb}\mathbf{H}_j$, where *Nb* is the number of neighboring cells surrounding the node. The normal vector can be easily calculated using the Gauss' formula, and index information of the mesh (*i*, *j*, *k* for the structured grid, and connectivity and neighboring cell for unstructured grid) provided from the grid generation tool.

3.4. Assessment of meta model

The meta model was first applied to predict ice thickness with a physical unit of millimeter (an order of 1) for the heat-on mode. The two-dimensional NACA 0012 airfoil used in the validation study was used as the reference geometry when assessing the ice thickness over the continuous maximum icing envelope in 14 CFR part 25 appendix C, power densities, and size of the heat pad. The grid topology and settings of the CFD solvers were the same as those used for the validation study of the airfoil. For the analysis of ice thickness on the solid surface, each snapshot consists of 362 nodes defining the surface mesh as a dimension per set of input. The accuracy of the meta solutions versus CFD solutions was evaluated using the LOOCV method. The maximum error between the meta and CFD solutions in the ice thickness was calculated as,

$$\varepsilon = \max_{i=1,\cdots,Ng}\left(\left|\left(H_{Meta}\right)_i - \left(H_{CFD}\right)_i\right|\right), \tag{13}$$

where *H* represents the ice thickness on each node of the anti-icing surfaces and *Ng* is the total number of nodes on the anti-icing surface. To build a meta model, it is essential to have enough number of samples, and a number of sampling techniques such as Latin hypercube sampling (LHS), random sampling, and uniform sampling, are available. In this study, uniform sampling for four different temperatures was used, and the initial and final samples (24 and 44) over the continuous maximum icing envelope were chosen, as shown in the left and the right of Fig. 14, respectively.

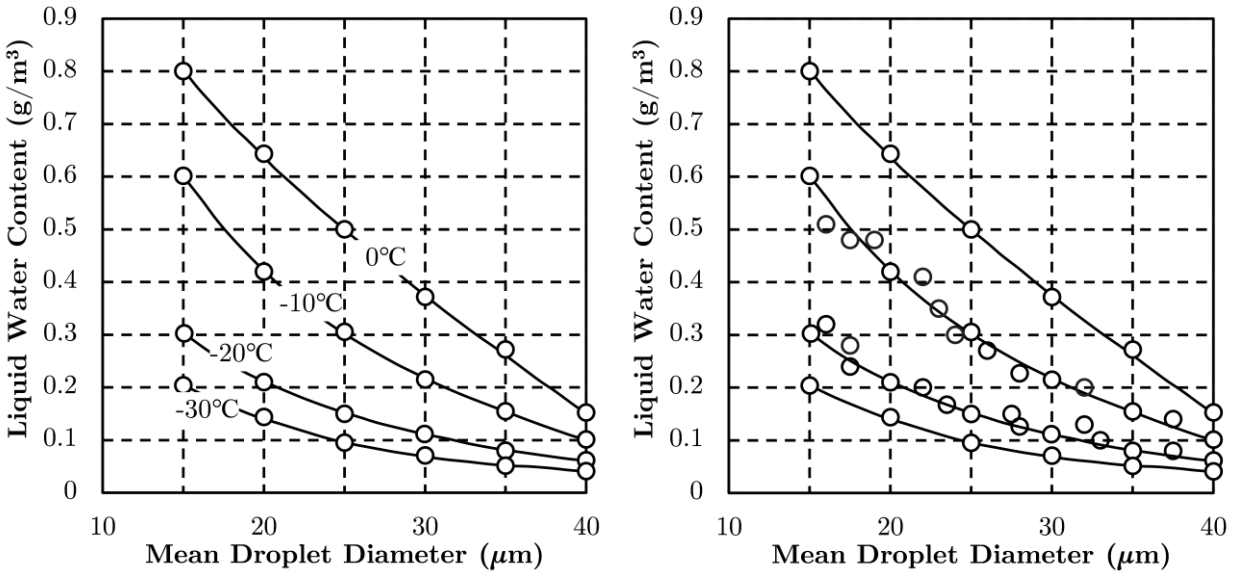

Fig. 14. Initial (left) and final (right) samples over the continuous maximum icing envelope for the meta model.

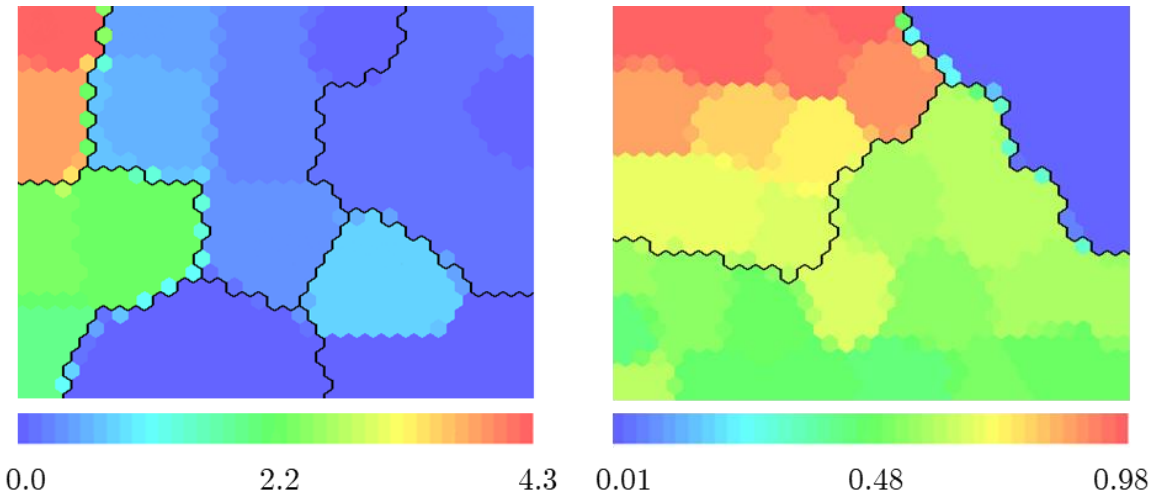

Fig. 15. Initial (left) and final (right) SOM analysis on the anti-ice surface using the LOOCV approach. The color map represents the maximum error between the meta and CFD solutions defined in Eq. (13) (unit=mm).

Figure 15 shows the initial (left) and final (right) SOM analysis using the LOOCV approach. The highest error of ice thickness is less than 1.0 mm in the final stage, and this error is acceptable to complete the meta model. The updated samples were chosen by k-mean clustering in the SOM analysis. Once the errors are clustered by the SOM, the MVD and LWC values corresponding to the clustered errors become the newly selected samples.

In this study, the newly selected samples were mainly distributed between the temperatures of -10 and -20 Celsius. These temperatures are generally recognized as the glaze icing condition, which can produce irregular ice shapes such as ice horns. Thus, more samples may be required to accurately capture the ice thickness in this range for the meta model. Ice accretions rarely occurred in the relatively high temperatures above the icing envelope, due to the heat-on mode of the anti-icing panel. When the atmospheric temperature decreased to the lowest temperature of -30 Celsius, the heating power of the heat-on mode for anti-icing was unable to evaporate the supercooled water droplets.

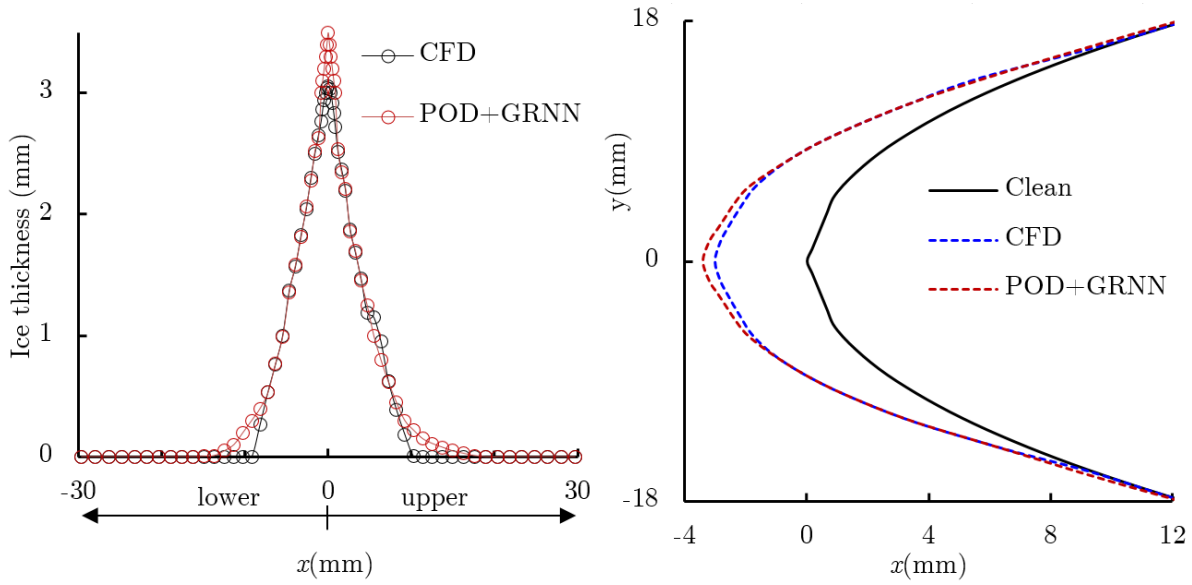

Fig. 16. Comparison of ice thickness (left) and ice shapes (right) between the meta and CFD solutions for heater power densities given in Table 1 (MVD=20μm, LWC=0.3017g/m^3, V=44.7m/s, T=-20°C).

The POD modes can be truncated at a specific energy content. In this analysis, the energy content of 99.9% was selected, and effective POD modes were updated from the initial five POD modes to a final seven POD modes. Figure 16 shows the ice thicknesses obtained from the meta model and the CFD solutions. The maximum error in ice thickness between the meta and CFD solutions was observed at the leading edge of the airfoil, and the magnitude of the error was approximately 0.5 mm. In the iced area on the airfoil surface, the meta model solution predicted a little larger ice thickness than the CFD solution. However, the differences may be ignored, since the resulting ice shapes of the meta and CFD solutions were in close agreement with each other, as shown in the right of Fig. 16.

4. Meta model for ice thickness on the anti-icing surface and its use in anti-icing certification

Evaluating the performance of anti-icing systems installed around a rotorcraft engine air intake in the heat-on mode during all-weather operations is a critical task in icing certification [51-54]. Direct CFD simulation with a high-performance computing system can be used to evaluate performance, but running such a simulation over the entire icing envelope requires enormous computational resources and time, rendering it unrealistic and not achievable in the near future. The meta model is an alternative, a way of circumventing this challenging computational issue. In this study, the continuous parametric space was assumed to be the continuous maximum icing condition defined in the 14 CFR part 25 Appendix C. The meta model for the rotorcraft engine air intake was first built using the CFD simulation results validated in subsection 3.2. The anti-icing zone around the ECS and nacelle shown in Fig. 10 was modified to incorporate the newly designed anti-icing panel. The anti-icing performance was then evaluated for the entire icing envelope. In particular, information about the high accumulation icing zone on the anti-icing surface and its corresponding parameters are presented to provide guidance for the proper design of anti-icing heater power and heat pad size.

4.1. Meta solutions of ice thickness

The meta model was built to predict ice thickness on the surface of the rotorcraft engine air intake in the heat-on mode. The rotorcraft engine air intake used in the validation study was considered to be the reference geometry for imposing the icing conditions, heater power, and size of the heat pad. The airflow conditions and the target mass flow rate were set to be a velocity of 65 m/s, an angle of sideslip of -2 degree, and a target mass flow rate of 3.8kg/sec at the end of the engine intake. The time exposed to the icing condition was assumed to be 500 seconds. The grid topology and settings of the CFD solvers were the same as those used in the validation study of the rotorcraft engine air intake.

The anti-icing zones were divided into three domains with different heat capacities. Figure 17 shows three anti-icing domains on the newly designed anti-icing panels. The major change was made on domain C where the size of the anti-icing panel around the ECS and nacelle was cut because the ice rarely accumulated around these areas because of the small mass flows and the positions aligned with a direction of flow streamlines. The meta models were allocated to each domain to reduce the computational cost, due to the large size of the matrix of the POD when all of the nodes on the anti-icing surfaces were considered to construct the POD. To build the meta model, uniform sampling was again used, as shown in the left of Fig. 14. The snapshots for domains A, B, C consisted of the 2,764, 3,351, and 256 nodes in the surface mesh, respectively. The accuracy of the meta solutions versus CFD solutions was evaluated using the LOOCV method. Equation (13) was adopted to define the maximum error in the ice thickness between the meta and CFD solutions. The energy content in equation (11) was defined as 99.9% for the selection of proper POD modes. Also, 7, 5, and 5 modes for each domain are selected for the initial samples.

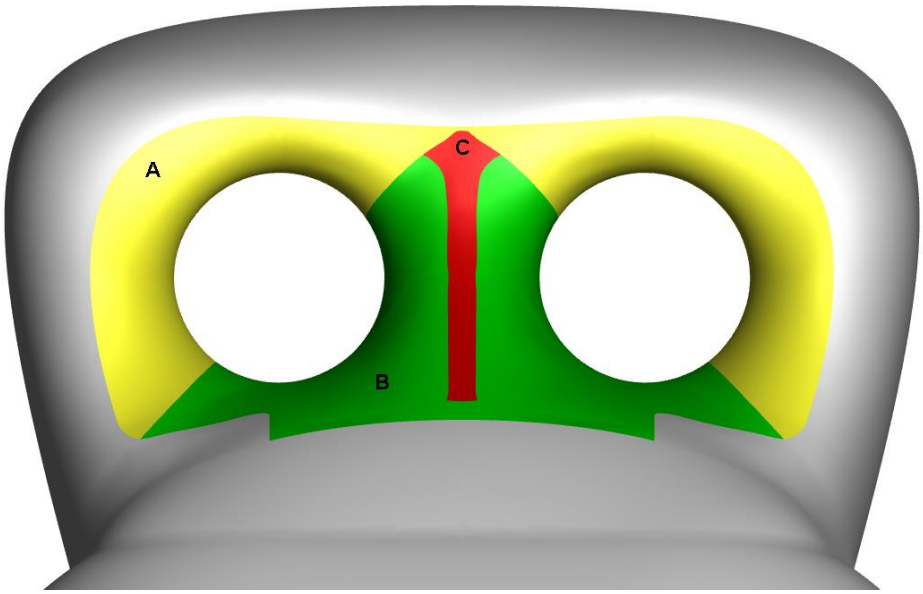

Fig. 17. Three anti-icing domains on the newly designed anti-icing panels around the rotorcraft engine air intake.

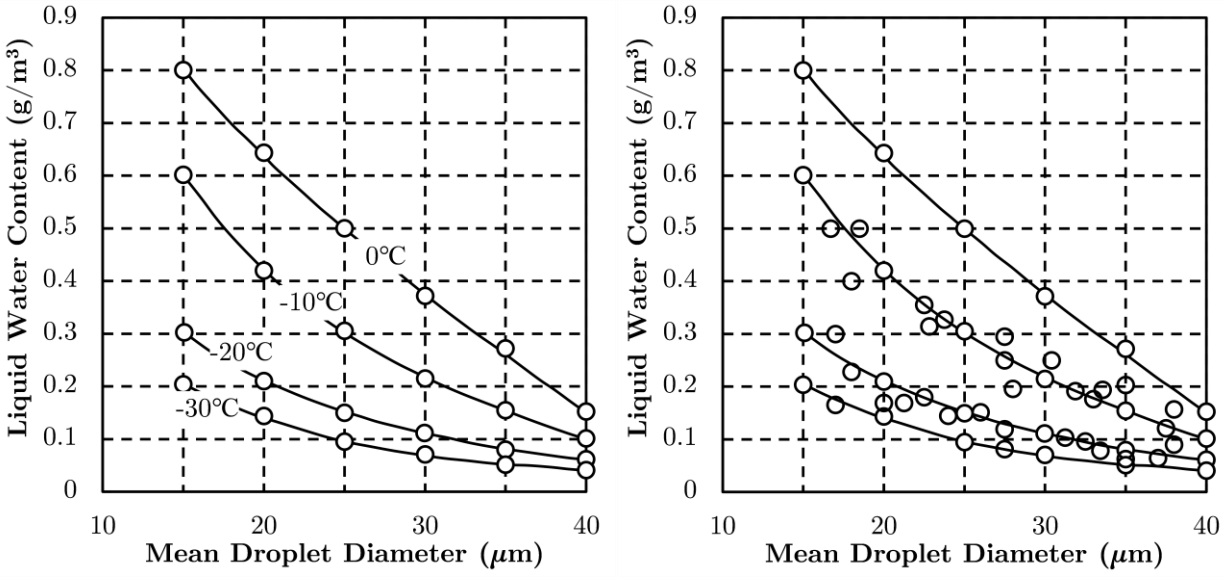

Fig. 18. Initial (left) and finally updated (right) samples for the meta model of the rotorcraft engine air intake anti-icing system.

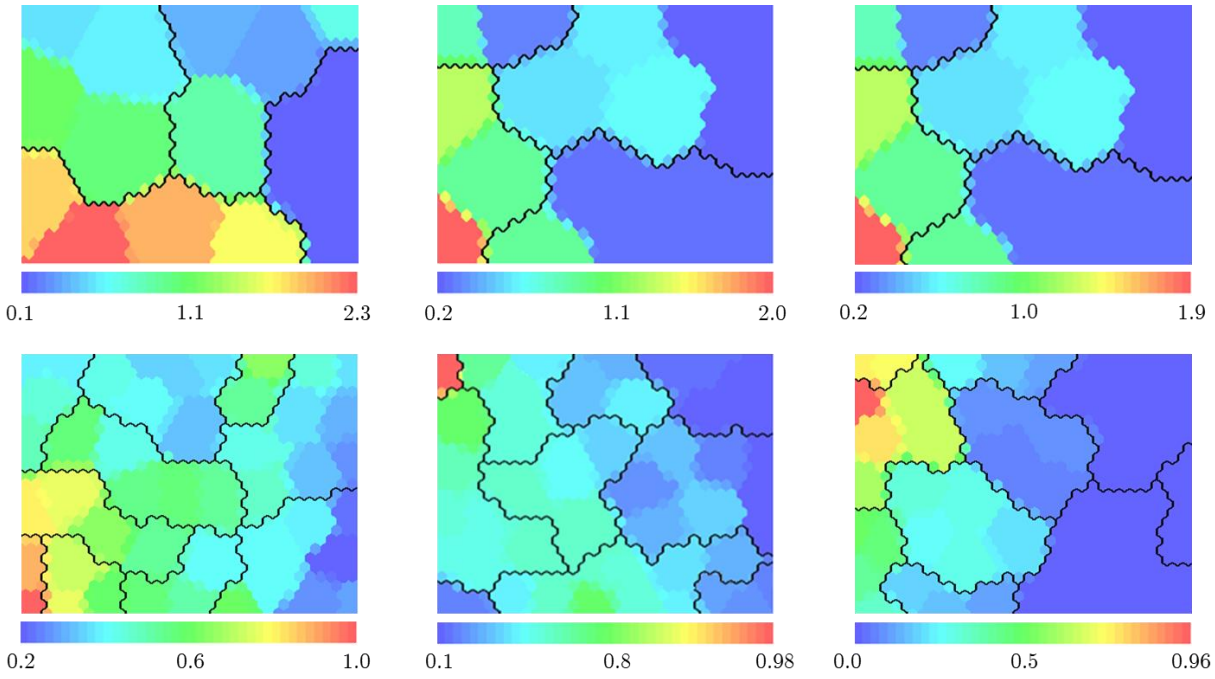

Fig. 19. Initial (up) and final (down) SOM analysis on the anti-ice surface using the LOOCV approach (unit=mm).

The clustering analysis for the error-driven iterative sampling was carried out using the SOM method. Newly updated samples were directly searched via the k-mean clustering of the SOM. Figure 18 shows the initial samples and finally updated samples. In the final stage, 54 snapshots are obtained via the SOM analysis. The maximum errors in the ice thickness at the initial and final stages are shown in Fig. 19. The maximum error was reduced by approximately 50 percent for each domain.

During the iteration, the effective POD modes (99.9% of the sum of POD modes) were also updated from the initial 7, 5, and 5 POD modes to the final 18, 7, and 5 POD modes for the A, B, C domains, respectively. The effective POD modes in domain A underwent a significant change, since a substantial amount of ice accumulated on domain A. In contrast, the other domains showed minor changes in the effective POD modes because there was less ice accretion in those domains. For example, even in the heat-off mode, ice rarely accumulated on domain B, as was already observed in previous experimental tests and

the CFD simulations shown in Fig. 11. For domain C, where the heater power was relatively high, the effective POD modes at the final stage remained exactly the same as the initially selected POD modes.

4.2. Use of the meta model for evaluating anti-icing performance

The present meta model solutions were accurate enough to predict the continuous space. The capability of the rotorcraft engine air intake anti-icing can therefore be evaluated for practical use using the meta model. In particular, information about the distributions of ice thickness on the anti-icing surfaces in the heat-on mode, heater power and the size of heat pads can be obtained to guide the design of the anti-icing system at the concept stage.

For this purpose, 6 temperature lines and 11 points for each temperature line were selected to analyze the ice thickness, as shown in Fig. 20. Temperature lines were selected since atmospheric temperature is a major factor when evaluating anti-icing performance around a rotorcraft engine air intake. If the heat-off mode is considered, the larger MVD and LWC at the relatively high temperature will play a key role in ice accretion. However, in the heat-on mode, water droplets tend to quickly evaporate at relatively high temperature conditions after impingement, due to the heater power. Based on this analysis, 6 temperature lines were selected for every 5 degrees Celsius, with 11 points for each temperature line. The 11 points were selected based on the MVD, from 15 micrometers to 40 micrometers at equal intervals of 2.5 micrometers. The resulting LWC values were determined as a function of the temperature and MVD.

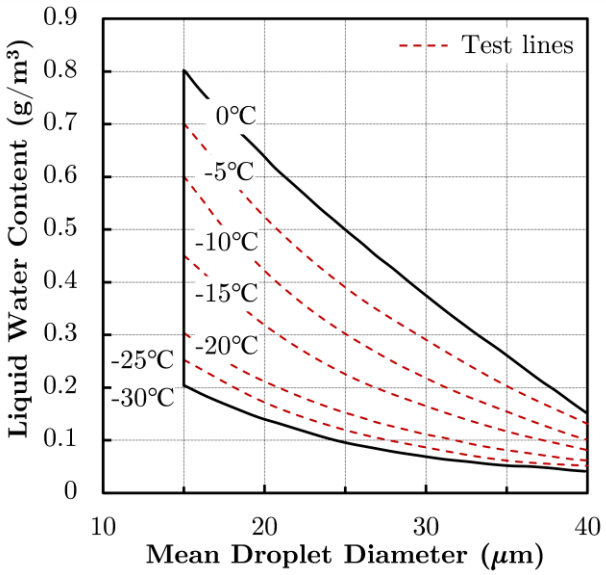

Fig. 20. Uniformly selected test lines in 14 CFR part 25 appendix C.

Figure 21 shows the distributions of ice thickness on the anti-icing surfaces at each temperature. This figure was obtained by over-plotting the areas (with ice thickness higher than 0.2 mm at least once) on the anti-icing surface as a contour map for 11 test points with different MVD values. The areas with ice thickness higher than 0.2 mm are shown, since they may affect engine performance. When the 14 CFR part 25 Appendix C was considered for the icing conditions (45 mins.), ice 0.2 mm thick at the given time (8.3 mins.) can reach 1 mm in the turbulent boundary layer around the rotorcraft engine air intake, which can be fully occupied by ice accretion. On this basis, ice thickness of 0.2 mm may be considered a criterion for determining potentially damaging areas.

At relatively high temperatures, such as cases (a) and (b) in Fig. 21, ice accretions occur in small regions around the boundary between zone A and the unprotected surfaces. The water films, which are non-evaporated water, move toward the upper side, and then form ice when the water films reach unprotected surfaces. As expected, in general the iced areas increase with decreasing temperature, as shown Fig. 21.

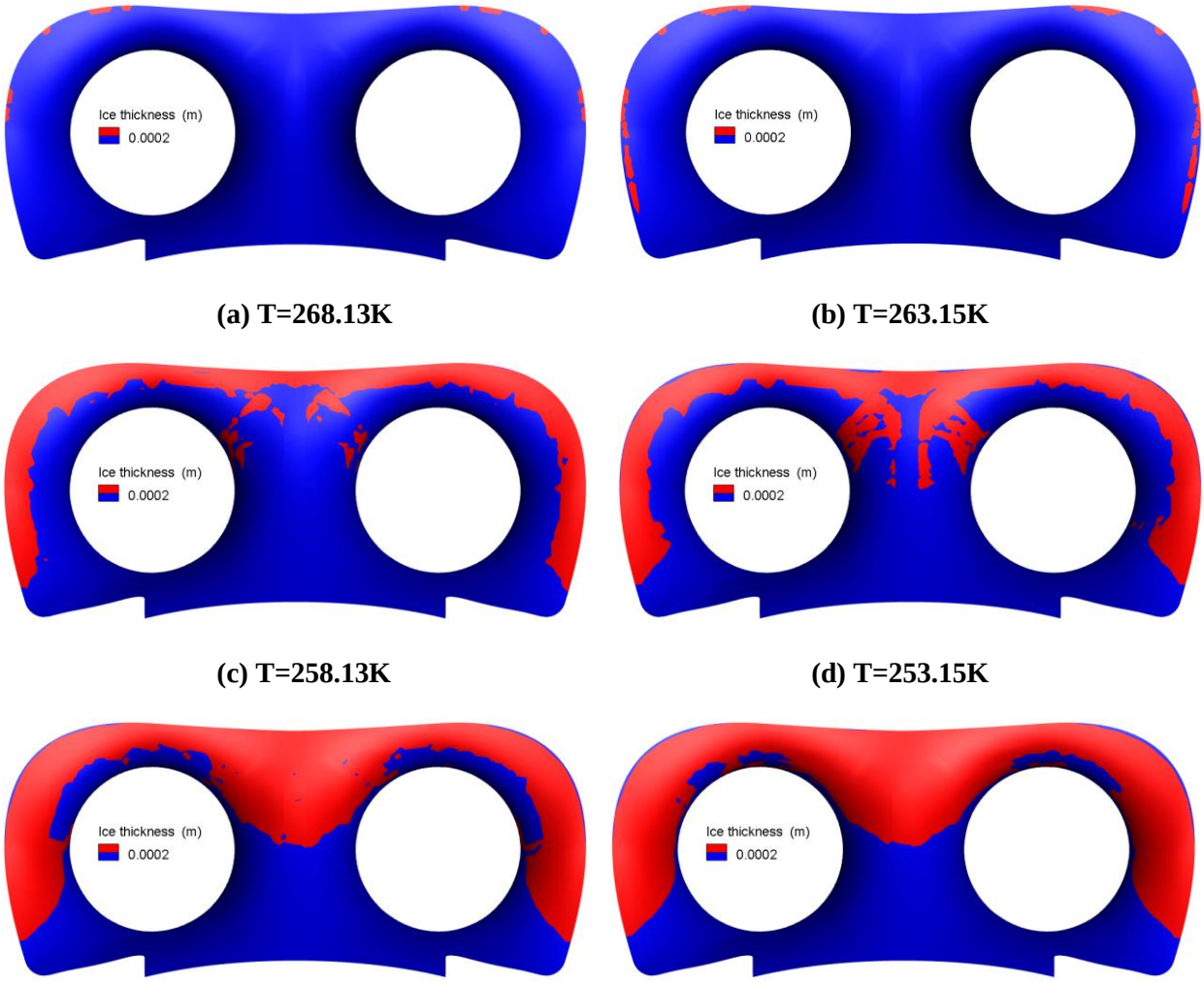

(a) T=268.13K **(b) T=263.15K**

(c) T=258.13K **(d) T=253.15K**

(e) T=248.13K **(f) T=243.15K**

Fig. 21. Distributions of ice thickness with uniformly selected test lines on the anti-icing surface around the rotorcraft engine air intake.

Interestingly, the heater power in domain C may be high enough to guarantee anti-icing performance until -20 ℃ (cases (c) and (d)), and the ice thickness above the 0.2 mm was rarely observed at the boundary between the domain A and C. The ice observed on domain B at temperatures of -10 and -20 ℃ may result from the water film on domains A and C. When the temperature further decreases (cases (e) and (f)), domains A and C are covered fully by ice, implying that the ice thickness on the anti-icing surface is highly dependent on temperature.

Figure 22 shows highly accumulated ice zones on the anti-icing surfaces, with an ice thickness resolution of 1 mm. This figure was obtained by over-plotting the thickness values for whole 66 test points (6 temperature lines and 11 points for each temperature line) on the anti-icing surface as a contour map, which is equivalent to select the maximum thickness at the locations. It can be noted that most of the ice has accumulated on domain A, and the thick ice with a thickness above 4 mm is located on the side edge of the domain A. In domain B, a relatively small amount of ice with a thickness of approximately 1 mm accumulated, in the zone where domains A and C meet. In domain C, the ice is accumulated on the small part of the domain. These findings indicate that careful attention should be paid to the arrangement of heating power and anti-icing panel in domain A.

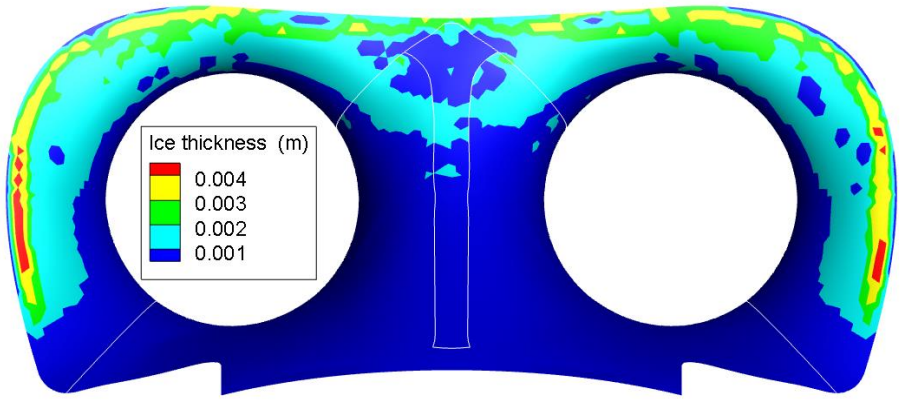

Fig. 22. Distributions of highly accumulated ice spots on the anti-icing surface around the rotorcraft engine air intake.

Figure 23 shows the temperature and MVD distributions corresponding to the highly accumulated ice zones shown in Fig. 22. This figure was obtained by two steps; 1) for a particular test point, the areas with ice thickness higher than 1 mm are assigned with corresponding values of temperature and MVD; 2) temperature and MVD values for whole 66 test points are over-plotted on the anti-icing surface as a contour map, which is equivalent to select the minimum temperature and the maximum MVD values at the locations. Interestingly, the maximum ice thickness (the red zones in Fig. 22) is observed around the temperature, -20 ℃, and the MVD, 30μm. An explanation is that larger amounts of ice form under a suitable combination

of critical icing conditions, such as a low-enough temperature (the non-evaporated water droplets), the MVD (high collection efficiency), and LWC (the appropriate amount of water content per unit volume).

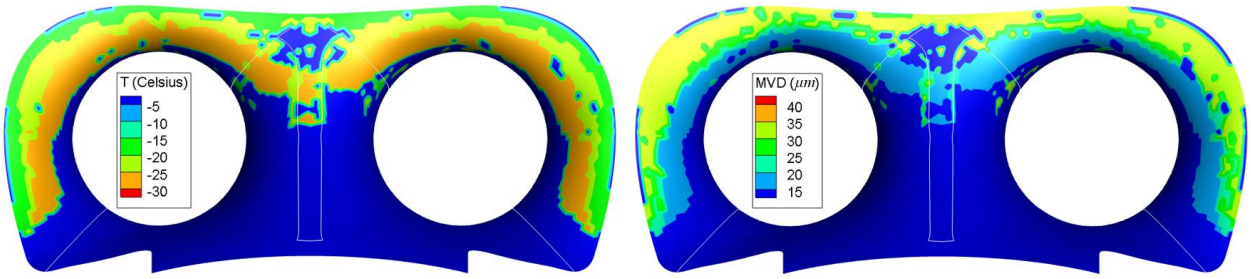

Fig. 23. Temperature (left) and MVD (right) distributions corresponding to the highly accumulated ice spots on the anti-icing surface around the rotorcraft engine air intake.

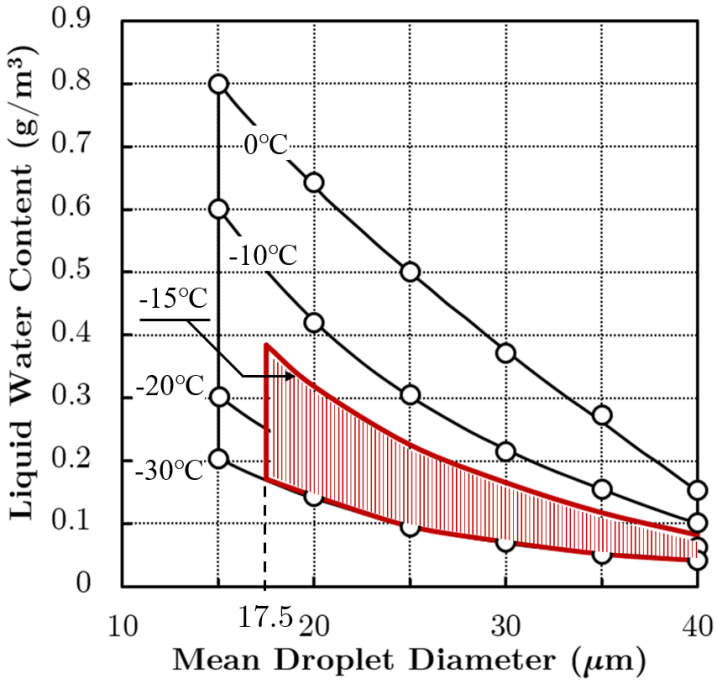

Fig. 24. Icing conditions corresponding to the highly accumulated ice spots on the anti-icing surface around the rotorcraft engine air intake.

Figure 23 also indicates a relationship among ice thickness, atmospheric temperature, and MVD, by which one can easily identify the critical atmospheric icing conditions around the rotorcraft engine air intake

under the given anti-icing capacity. An example of this relationship is shown in Fig. 24. According to Figs. 22 and 23, the present anti-icing capacity is not enough and more heat power is needed to evaporate the supercooled water droplets in critical icing conditions when the temperature is below -15 ℃ and the MVD is greater than 17.5μm, as illustrated by the red box in Fig. 24. Once such critical icing conditions are identified, the heat power and the size of heat pads can be easily rearranged by repeating the processes summarized in Figs. 20-24, using the meta model.

5. Conclusions

The accuracy of the meta model depends critically on the reliability of the original data set. Even though the meta model is well established, the meta solutions cannot be guaranteed unless the reliability of the original date set is secure. In this study, two test cases were chosen to validate the CFD solutions, a two-dimensional NACA 0012 airfoil, and a three-dimensional rotorcraft engine air intake. The CFD solutions were shown to be in good agreement with the experimental data. The same procedure developed to validate the CFD solutions was then applied to produce data sets for the meta model. In addition, a meta model for predicting the ice thickness on the anti-icing surfaces was developed by employing the reduced-order model with proper orthogonal decomposition and general regression neural network. The self-organized map and leave-one-out cross-validation approaches were also used to update new samples and assess the meta model, respectively.

All of these efforts were intended to develop a design criterion for continuous parametric spaces from discretized parametric space, which is closely related to computational efficiencies. Based on the results of the present study, the meta model was found capable of fulfilling the continuous parametric space and suitable for practical use in evaluating anti-icing performance. In the sample test case, a critical zone with highly accumulated ice was identified on domain A, and the corresponding icing conditions of a temperature below -15 ℃ and an MVD greater than 17.5μm, were identified under the given heating power of the rotorcraft.

Several topics remain that require further investigation. First, there is issue of the proper number of new snapshots that should be introduced with each iteration. The SOM analysis provides clustered zones using the errors obtained from the LOOCV module, but the number of new samples to be added heavily depends on the number of clustering zones that the user sets up. Second, there is issue of how well the meta model and CFD solvers can cope with significant growth of ice shapes affecting the flow locally, in the case of the melted ice (water film) on the unprotected surfaces at a glaze icing condition. Third, there is a strong need to extend the present method to the optimization of the anti-icing system design. The present meta model may need to improve the accuracy of the predicted solutions for providing feasible data during the optimization process. For example, accuracy of predictions on regions without ice growth due to an abundance of heating power needs to be enhanced in order to find the minimum required power to prevent problematic ice accretion. Fourth, intermittent maximum icing (IMI) conditions with subsequent continuous maximum icing (CMI) conditions (or in reversed order) could be an interesting case. This case is part of a full commercial icing certification process. Short durations of increased LWC during IMI could reduce the surface temperature substantially and initiate ice accretion. Lastly, the meta model needs to be extended to handle ice accretion of supercooled large droplets (SLD), which was formally introduced as appendix O in November 2014.

Acknowledgments

This work was supported by the National Research Foundation of Korea (NRF) Grant funded by the Ministry of Science, ICT & Future Planning (NRF-2017-R1A5A1015311), South Korea. The authors thank the referees of this paper for their valuable and very helpful comments and suggestions.

References

[1] W.M. Schulze, Aircraft engine inlet cowl anti-icing system, US Patent US005088277A (1992).
[2] R.J. Kind, M.G. Potapczuk, A. Feo, C. Golia, A.D. Shah, Experimental and computational simulation of in-flight icing phenomena, Progress in Aerospace Sciences 34 (1998) 257–345.

[3] R.W. Gent, N.P. Dart, J.T. Cansdale, Aircraft icing, Philosophical Transactions of the Royal Society of London Series A: Mathematical and Physical Sciences 358 (2000) 2873–2911.
[4] Y. Cao, K. Chen, Helicopter icing, Aeronautical Journal 114 (2010) 83–90.
[5] O. Meier, D. Scholz, A handbook method for the estimation of power requirements for electrical de-icing systems, DLRK ID161191 (2010).
[6] G.B. Ahn, K.Y. Jung, R.S. Myong, H.B. Shin, W.G. Habashi, Numerical and experimental investigation of ice accretion on rotorcraft engine air intake, Journal of Aircraft 52 (2015) 903–909.
[7] Y. Cao, C. Ma, Q. Zhang, J. Sheridan, Numerical simulation of ice accretions on an aircraft wing, Aerospace Science and Technology 23 (2012) 296–304.
[8] M. Mirzaei, M.A. Ardekani, M. Doosttalab, Numerical and experimental study of flow field characteristics of an iced airfoil, Aerospace Science and Technology 13 (2009) 267–76.
[9] A. Lampton, J. Valasek, Prediction of icing effects on the lateral/directional stability and control of light airplanes, Aerospace Science and Technology 23 (2012) 305–11.
[10] T. Liu, K. Qu, J. Cai, S. Pan, A three-dimensional aircraft ice accretion model based on the numerical solution of the unsteady Stefan problem, Aerospace Science and Technology 93 (2019) 105328.
[11] L. P. Raj, K. Yee, R.S. Myong, Sensitivity of ice accretion and aerodynamic performance degradation to critical physical and modeling parameters affecting airfoil icing, Aerospace Science and Technology 98 (2020) 105659.
[12] J. Wang, Z. Lu, Y. Shi, Aircraft icing safety analysis method in presence of fuzzy inputs and fuzzy state, Aerospace Science and Technology 82–83 (2018) 172–184.
[13] E.S. Ayra, A.R. Sanz, R.A. Valdes, F.G. Comendador, J. Cano, Detection and warning of ice crystals clogging pitot probes from total air temperature anomalies, Aerospace Science and Technology 102 (2020) 105874.
[14] BEA, On the accident on 1st June 2009 to the Airbus A330-203 registered F-GZCP operated by Air France flight AF 447 Rio de Janeiro-Paris, Tech. Rep., BEA -Bureau d'Enqutes et d'Analyses pour la sécurité de l'aviation civile (BEA), 2009, URL, https://www.bea.aero/docspa/2009/f-cp090601.en/pdf/f-cp090601.en.pdf.
[15] K.M. Al-Khalil, T.G. Keith Jr., K.J. De Witt, J.K. Nathman, D.A. Dietrich, Thermal analysis of engine inlet anti-icing systems, Journal of Propulsion and Power 6 (1990) 628–634.
[16] K.M. Al-Khalil, T.G. Keith Jr., K.J. De Witt, Icing calculations on a typical commercial jet engine inlet nacelle, Journal of Aircraft 34 (1997) 87–93.

[17] T.G. Keith Jr., K.J. De Witt, W.B. Wright, K.C. Masiulaniec, Overview of numerical codes developed for predicted electrothermal de-icing of aircraft blades, in: 26th Aerospace Meeting, American Institute of Aeronautics and Astronautics, 1988.
[18] G.A.L. Silva, O.M. Silvares, E.J.G.J. Zerbini, Airfoil anti-ice system modeling and simulation, in: 41th Aerospace Meeting and Exhibit, American Institute of Aeronautics and Astronautics, 2003.
[19] W.B. Wright, T.G. Keith Jr., K.J. De Witt, Numerical simulation of icing, deicing, and shedding, in: 29th Aerospace Science and Meeting, American Institute of Aeronautics and Astronautics, 1991.
[20] S. Nishio, S. Kato, Development of ice accretion and anti- icing system simulation code, in: 24th International Congress of the Aeronautical Sciences, International Council of the Aeronautical Sciences, 2004.
[21] Y. Lin, H. Chen, G. Wang, A. Liu, Recent progress in preparation and anti-icing applications of superhydrophobic coatings, Coatings 8 (2018) 208.
[22] Y. Shen, X. Wu, J. Tao, C. Zhu, Y. Lai, Z. Chen, Icephobic materials: Fundamentals, performance evaluation, and applications, Progress in Materials Science 103 (2019) 509–557.
[23] D.J. Lucia, P.S. Beran, W.A. Silva, Reduced-order modeling: New approaches for computational physics, Progress in Aerospace Sciences 40 (2004) 51–117.
[24] P. Holmes, J.L. Lumley, G. Berkooz, Turbulence, Coherent Structures, Dynamical Systems and Symmetry, Cambridge University Press, 1996.
[25] L. Sirovich, Turbulence and the dynamics of coherent structures. I. Coherent structures, Quarterly of Applied Mathematics 45 (1987) 561–571.
[26] M. Fossati, W.G. Habashi, Multiparameter analysis of aero-icing problems using proper orthogonal decomposition and multidimensional interpolation, AIAA Journal 51(4) (2013) 946–960.
[27] X. Bu, R. Yang, J. Yu, X. Shen, G. Lin, Fast algorithm for prediction of airfoil anti-icing heat load, Energy and Power Engineering 5 (2013) 493–497.
[28] S.K. Jung, S.M. Shin, R.S. Myong, T.H. Cho, An efficient CFD-based method for aircraft icing simulation using a reduced order model, Journal of Mechanical Science and Technology 25 (2011) 703–711.
[29] S.K. Jung, R.S. Myong, T.H. Cho, Development of Eulerian droplets impingement model using HLLC Riemann solver and POD-based reduced order method, in:41st AIAA Fluid Dynamics Conference and Exhibit, American Institute of Aeronautics and Astronautics, 2011.
[30] Z.L. Li, M. Yang, X. Luo, J. Zhang, M.N. Yuan, A spline ROM of blade aerodynamic force to upstream wake, Aerospace Science and Technology 84 (2019) 650–660.

[31] H. Kwon, S. Choi, A trended Kriging model with R2 indicator and application to design optimization, Aerospace Science and Technology 43 (2015) 111–125.
[32] C. Audouze, F. DeVuyst, P.B. Nair, Reduced-order modeling of parameterized PDEs using time-space-parameter principal component analysis, International Journal for Numerical Methods in Engineering. 80 (2009) 1025–1057.
[33] T. Bui-Thanh, M. Damodaran, K. Willcox, Aerodynamic data reconstruction and inverse design using proper orthogonal decomposition, AIAA Journal 42 (2004) 1505–1516.
[34] X. Li, A.C. Zecchin, H.R. Maier, Selection of smoothing parameter estimators for general regression neural networks: Applications to hydrological and water resources modelling, Environmental Modelling and Software 59 (2014) 162-86.
[35] A.E. Ben-Nakhi, M.A. Mahmoud, Cooling load prediction for buildings using general regression neural networks, Energy Conversion and Management 45 (2004) 2127–2141.
[36] Z. Zhan, W.G. Habashi, M. Fossati, Local reduced-order modeling and iterative sampling for parametric analyses of aero-icing problems, AIAA Journal 53 (2015) 2174–2185.
[37] S.K. Jung, W. Choi, M-F. Luiz S., M. Fernando, An implementation of self organizing maps for airfoil design exploration via the multi-objective optimization technique, Journal of Aerospace Technology and Management 8 (2016) 193–202.
[38] T. Bui-Thanh, K. Willcox, O. Ghattas, Parametric reduced-order models for probabilistic analysis of unsteady aerodynamic applications, AIAA Journal 46 (2008) 2520–2529.
[39] A. Paul-Dubois-Taine, D. Amsallem, An adaptive and efficient greedy procedure for the optimal training of parametric reduced-order models, International Journal for Numerical Methods in Engineering 102 (2015) 1262–1292.
[40] A. Du, V. Faber, M. Gunzburger, Centroidal Voronoi tessellations: Applications and algorithms, SIAM Review 41 (1999) 637–676.
[41] R. Heise, Implementation of a two-stream-fan in the CIRSTEL system, Ph.D. Thesis, University of Stellenbosch, 2006.
[42] S.K. Jung, R.S. Myong, A second-order positivity-preserving finite volume upwind scheme for air-mixed droplet flow in atmospheric icing, Computers and Fluids 86 (2013) 459–469.
[43] L.P. Raj, J. Lee, R.S. Myong, Ice accretion and aerodynamic effects on a multi-element airfoil under SLD icing conditions, Aerospace Science and Technology 85 (2019) 320–333.
[44] G. Croce, H. Beaugendre, W. Habashi, CHT3D - FENSAP-ICE conjugate heat transfer computations with droplet impingement and runback effects, AIAA-2002-0386, 2002.
[45] T. Kohonen, Self-organizing Maps, Springer, 1995.

[46] J. Hollmen, V. Tresp, O. Simula, A self-organizing map for clustering probabilistic models, in: 9th International Conference on Artificial Neural Networks, Institute of Electrical and Electronics Engineers, 1999.
[47] K.M. Al-Khalil, C. Horvath, R. Miller, W.B. Wright, Validation of NASA thermal ice protection computer codes, Part 3: The validation of Antice, NASA/TM 210907, 2001.
[48] NASA Langley Turbulence Modeling Resource web site, 2D NACA 0012 Airfoil Validation Case: https://turbmodels.larc.nasa.gov/naca0012numerics_val.html, 2018.
[49] G. Silva, O. Silvares, E. Zerbini, Water film breakdown and rivulets formation effects on thermal anti-ice operation simulation, AIAA-2006-3785, 2006.
[50] Z. Zhan, W.G. Habashi, M. Fossati, Real-time regional jet comprehensive aeroicing analysis via reduced-order modeling, AIAA Journal 54 (2016) 3787–3802.
[51] S. van't Hoff, J. van der Vorst, R.J. Flemming, D. Parkins, Icing certification of Korean utility helicopter KUH-1: Artificial icing flight test, AIAA-2017-3930, 2017.
[52] K. Lammers, S. van't Hoff, H. Ferschitz, M. Wannemacher, Helicopter engine air intake icing wind tunnel certification test, NLR-TP-2018-434, 2018.
[53] A.C. de Bruin, G. Fatigati, H.B. Shin, KAI Surion helicopter full-scale air intake testing at CIRA Icing Wind Tunnel, NLR-TP-2016-491, 2016.
[54] S. van't Hoff, K. Lammers, Y.S. Hwang, J.S. Kim, K.S. Kim, Korean utility helicopter KUH-1 icing certification program. SAE International Journal of Advances and Current Practices in Mobility 2(1) (2020) 205–215.